

Strong Coupling of Hydrodynamics and Reactions in Nuclear Statistical Equilibrium for Modeling Convection in Massive Stars

MICHAEL ZINGALE,¹ ZHI CHEN,¹ ERIC T. JOHNSON,¹ MAX P. KATZ,¹ AND ALEXANDER SMITH CLARK¹

¹*Department of Physics and Astronomy, Stony Brook University, Stony Brook, NY 11794-3800, USA*

ABSTRACT

We build on the simplified spectral deferred corrections (SDC) coupling of hydrodynamics and reactions to handle the case of nuclear statistical equilibrium (NSE) and electron/positron captures/decays in the cores of massive stars. Our approach blends a traditional reaction network on the grid with a tabulated NSE state from a very large, $\mathcal{O}(100)$ nuclei, network. We demonstrate how to achieve second-order accuracy in the simplified-SDC framework when coupling NSE to hydrodynamics, with the ability to evolve the star on the hydrodynamics timestep. We discuss the application of this method to convection in massive stars leading up to core-collapse. We also show how to initialize the initial convective state from a 1D model in a self-consistent fashion. All of these developments are done in the publicly available *Castro* simulation code and the entire simulation methodology is fully GPU accelerated.

Keywords: hydrodynamics—methods: numerical—nucleosynthesis

1. INTRODUCTION

When modeling reactive flows in stars, the energy release from nuclear reactions drives a variety of complex behaviors, including convection, flames, and detonations. In massive stars, during the final approach to a core-collapse supernova, capturing the energy release can be especially challenging as the Si burning is very energetic and, in the core, a large number of electron-capture reactions need to be accounted for. This demands a large reaction network, which is computationally expensive in multi-dimensions. The direct feedback between the reactions and the hydrodynamics means that care needs to be taken to ensure that the reactions and hydrodynamics are properly coupled together. The difficulty in doing this stems from the fact that explicit-in-time integration is usually preferred for hydrodynamics while implicit methods are usually needed for reactions due to their stiff nature. Traditionally, an operator splitting approach has been used to update the fluid state in time.

One-dimensional models of massive star evolution leading to core-collapse can use hundreds of nuclei (e.g. [Rauscher et al. 2002](#)) including important electron/positron captures and decays ([Heger et al. 2001](#)), allowing for detailed evolution of the electron fraction in the iron core. In contrast, most multidimensional models of massive star convection use smaller networks, like the standard 21-nuclei `aprox21` network,

as their workhorse. These smaller networks may not be able to capture the energetics and nucleosynthesis (Navó et al. 2023).

Multidimensional models of massive star evolution have explored a variety of progenitor masses, focusing on different aspects of the evolution, with a range of different algorithms, including differences in the grid geometry, evolution of the core, and reaction network (and its integration). Here we summarize these differences, focusing on the geometry and treatment of the core.

The work of Arnett & Meakin (2011) considered 2D simulations of the C, Ne, O, and Si shells, using a reaction network with 38 species. They showed that large asymmetries in the burning shells can form, in contrast to the classic “onion skin” picture from one-dimensional models. This work used spherical coordinates and cut out the inner iron core.

Couch et al. (2015); Chatzopoulos et al. (2016); Fields & Couch (2020, 2021) looked at the late stages of convection leading up to core collapse in 3D with a variety of progenitors, using the `aprox21` network. These all used a Cartesian geometry, with differing treatments of the iron core. In Fields & Couch (2020, 2021), the evolution of the core was done by interpolating the evolution from the one-dimensional MESA model, acting as an effective inner boundary condition. Due to the operator splitting of hydrodynamics and reactions, they also used a reaction-based timestep, only allowing the internal energy to change by 1% per timestep.

Other recent work used 3D spherical geometry with the core not modeled (Müller et al. 2017; Varma & Mueller 2023), or 3D with the core evolved in 1D with spherical symmetry (Yoshida et al. 2019, 2021b,a). The `aprox21` network in Yoshida et al. (2021b) transitioned to nuclear statistical equilibrium (NSE) at high temperatures, similar to the approach that we will discuss here. An alternate 3D yin-yang geometry was used by Yadav et al. (2020), again with the core cutout.

All of these works have shown that asymmetries can have important impacts on the core-collapse explosion mechanism (see also Müller 2020). Capturing the evolution of the core is difficult however, both due to the coordinate singularity in some discretizations as well as the differing timescales of the reactions in the core versus the convective shells. Additionally, many weak interactions are important in the evolution of the electron fraction in the core that cannot be captured with a simple network.

Our goal here is to show how to model a massive star on the hydrodynamics timescale, instead of restricting the timestep based on the energy release, by using strongly-coupled time-integration strategies. We also aim to self-consistently evolve the core by capturing the NSE state, and show how to do this with second-order accuracy. Finally, we show how to establish an initial convective velocity field from a 1D model. Since our focus here is on the time-integration algorithm, we work in a 2D axisymmetric geometry.

In Zingale et al. (2022) (henceforth Z22), we introduced a coupling method for hydrodynamics and reactions based on the ideas of spectral deferred corrections (SDC) (Dutt et al. 2000; Minion 2003; Zingale et al. 2019), but designed to work with the standard characteristic-tracing approach to hydrodynamics used in the corner transport upwind (CTU) (Colella 1990) method and its extension to the piecewise parabolic method (PPM) (Colella & Woodward 1984; Miller & Colella 2002). We termed this integration method “simplified-SDC”. With operator splitting, when the reactions are evolved, the “pdV” expansion is not seen. This means that if a lot of heat is released into a zone in a timestep, we will not see the expansion and cooling that should accompany this. In contrast to operator splitting, in SDC the advection and reactions explicitly see the effects of each other, and in Z22, we showed that this allows us to model explosive reactive flows more accurately and efficiently.

2. NUMERICAL METHODOLOGY

In this section, we will describe how to augment the equations of reacting hydrodynamic flow to accommodate the composition variables needed from NSE, and perform the coupled time-integration of the system. We use the **Castro** compressible astrophysics simulation code (Almgren et al. 2010; Almgren et al. 2020) together with the **AMReX** adaptive mesh refinement library (Zhang et al. 2019). We will follow the notation from Z22 and the composition approach of Ma et al. (2013). For simplicity, we write things out for a one-dimensional system, but the extension to multi-dimensions is straightforward.

The conservative-form of the one-dimensional reactive Euler equations can be written as:

$$\frac{\partial \mathbf{U}}{\partial t} + \frac{\partial \mathbf{F}(\mathbf{U})}{\partial x} = \mathbf{S}(\mathbf{U}) \quad (1)$$

with the conserved state

$$\mathbf{U} = (\rho, \rho X_k, \rho \alpha_l, \rho u, \rho E, \rho e)^\top \quad (2)$$

where ρ is the mass density, u is velocity, E is specific total energy, e is the specific internal energy, X_k are the mass fractions, subject to $\sum_k X_k = 1$, and α_l are auxiliary composition variables. Following Ma et al. (2013), we carry three auxiliary composition variables: electron fraction, Y_e ,

$$Y_e = \sum_k \frac{Z_k X_k}{A_k} \quad (3)$$

where A_k and Z_k are the atomic weight and atomic number of nucleus k , mean molecular weight, \bar{A} ,

$$\bar{A} = \left[\sum_k \frac{X_k}{A_k} \right]^{-1}, \quad (4)$$

and average binding energy per nucleon, $\langle B/A \rangle$:

$$\left\langle \frac{B}{A} \right\rangle = \sum_k \frac{B_k X_k}{A_k}, \quad (5)$$

where B_k is the binding energy of nucleus k . These same composition variables are used in the NSE implementation of Townsley et al. (2007). Finally, the specific total energy and specific internal energy are related via:

$$E = e + u^2/2 \quad (6)$$

The corresponding hydrodynamical fluxes are:

$$\mathbf{F}(\mathbf{U}) = \begin{pmatrix} \rho u \\ \rho X_k u \\ \rho \alpha_l u \\ \rho u^2 + p \\ (\rho E + p)u \\ \rho e u \end{pmatrix} \quad (7)$$

where p is the pressure. We separately evolve ρe , as part of a dual energy formalism (Bryan et al. 1995; Katz et al. 2016), and (ρe) evolution equation includes an additional “pdV” term that accounts for the variation of internal energy due to compression of the fluid element:

$$\frac{\partial(\rho e)}{\partial t} + \frac{\partial F(\rho e)}{\partial x} + p \frac{\partial u}{\partial x} = S_{\rho e} \quad (8)$$

Again following [Zingale et al. \(2022\)](#), we split the source term into hydrodynamic and reactive parts:

$$\mathbf{G}(\mathcal{U}) = \begin{pmatrix} 0 \\ 0 \\ 0 \\ \rho g \\ \rho u g \\ 0 \end{pmatrix} \quad \mathbf{R}(\mathcal{U}) = \begin{pmatrix} 0 \\ \rho \dot{\omega}_k \\ \rho \dot{\omega}_l \\ 0 \\ \rho \epsilon \\ \rho \epsilon \end{pmatrix} \quad (9)$$

with

$$\mathbf{S}(\mathcal{U}) = \mathbf{G}(\mathcal{U}) + \mathbf{R}(\mathcal{U}). \quad (10)$$

where g is the gravitational acceleration. Here, $\dot{\omega}_k$ is the creation rate for species k , $\dot{\omega}_l$ is the creation rate for auxiliary composition variable l , and ϵ is the energy generation rate per unit mass (we labeled this \dot{S} in Z22). We note that although we set $G_{\rho e}$ and $G_{\rho E}$ to zero for the current application, it could also include conductive radiation-transport terms. These reactive sources all depend on density, temperature, and composition. Finally, we define an advective term including the hydrodynamic sources:

$$\mathcal{A}(\mathcal{U}) = -\frac{\partial \mathbf{F}(\mathcal{U})}{\partial x} + \mathbf{G}(\mathcal{U}) \quad (11)$$

and again, the (ρe) component is treated specially:

$$\mathcal{A}(\rho e) = -\frac{\partial F(\rho e)}{\partial x} - p \frac{\partial u}{\partial x} + G_{\rho e} \quad (12)$$

The equation of state we use in this work takes a slightly different algebraic form than that in Z22 because of how we define the composition. For a system where the composition is completely specified by the mass fractions, X_k , the equation of state would take the form:

$$p = p(\rho, X_k, e); \quad T = T(\rho, X_k, e) \quad (13)$$

In this work, we will instead use the auxiliary composition variables, α_l , and the EOS has the form:

$$p = p(\rho, \alpha_l, e); \quad T = T(\rho, \alpha_l, e) \quad (14)$$

We use the Helmholtz stellar equation of state of [Timmes & Swesty \(2000\)](#); [Fryxell et al. \(2000\)](#) for all simulations here.

Our primitive variable system is also slightly different than that of Z22 because of the α_l term. The primitive variables are:

$$\mathbf{q} = (\rho, X_k, \alpha_l, u, p, (\rho e))^T \quad (15)$$

and writing the system as:

$$\mathbf{q}_t + \mathbf{A}^{(x)}(\mathbf{q})\mathbf{q}_x = \mathbf{S}(\mathbf{q}) \quad (16)$$

we have the matrix $\mathbf{A}^{(x)}$:

$$\mathbf{A}^{(x)}(\mathbf{q}) = \begin{pmatrix} u & 0 & 0 & \rho & 0 & 0 \\ 0 & u & 0 & 0 & 0 & 0 \\ 0 & 0 & u & 0 & 0 & 0 \\ 0 & 0 & 0 & u & 1/\rho & 0 \\ 0 & 0 & 0 & \Gamma_1 p & u & 0 \\ 0 & 0 & 0 & \rho h & 0 & u \end{pmatrix} \quad (17)$$

where h is the specific enthalpy and Γ_1 is an adiabatic index, $\Gamma_1 = d \log p / d \log \rho|_s$ at constant entropy. This form of the equations is used in the construction of the interface states and the characteristic decomposition of the jumps that reach the interface over the timestep. Similar to conservative variables we decompose the source terms, $\mathbf{S}(\mathbf{q})$ as:

$$\mathbf{S}(\mathbf{q}) = \mathbf{G}(\mathbf{q}) + \mathbf{R}(\mathbf{q}) \quad (18)$$

with

$$\mathbf{G}(\mathbf{q}) = \begin{pmatrix} 0 \\ 0 \\ 0 \\ g \\ 0 \\ 0 \end{pmatrix} \quad \mathbf{R}(\mathbf{q}) = \begin{pmatrix} 0 \\ \dot{\omega}(X_k) \\ \dot{\omega}(\alpha_l) \\ 0 \\ \Gamma_1 p \sigma \epsilon \\ \rho \epsilon \end{pmatrix} \quad (19)$$

where σ is

$$\sigma \equiv \frac{\partial p / \partial T|_\rho}{\rho c_p \partial p / \partial \rho|_T} \quad (20)$$

with c_p as the specific heat at constant pressure, $c_p = \partial h / \partial T|_p$. (see [Almgren et al. 2008](#)).

2.1. Overview of the simplified-SDC approach

The main idea of the simplified-SDC approach is that the hydrodynamics update explicitly sees a reactive source term and that the reaction network integration includes an advective term—this strongly couples the two processes and avoids the splitting error seen in the commonly used Strang operator splitting approach ([Strang 1968](#); [Zingale et al. 2021](#)). The full algorithm is described in Z22. The overall update is iterative, so we use the superscript (k) below to denote the iteration. The essential steps of the update are:

- *Create the advective update term, $[\mathcal{A}(\mathbf{u})]^{n+1/2,(k)}$, using the CTU PPM method ([Colella 1990](#); [Miller & Colella 2002](#)).* The interface states will see a source term in the prediction step that takes the form:

$$\mathbf{S}(\mathbf{q}) = \mathbf{G}(\mathbf{q}) + \mathcal{I}_{\mathbf{q}}^{n+1/2,(k-1)} \quad (21)$$

where $\mathcal{I}_{\mathbf{q}}^{n+1/2,(k-1)}$ is an approximation to the integral of the reaction sources over the timestep. In the first iteration, this is the source term from the previous step, in subsequent iterations, it is the source from the previous iteration.

- *Update the system using an ODE integrator.* We update the entire advection-reaction system as:

$$\frac{d\mathbf{u}}{dt} = [\mathcal{A}(\mathbf{u})]^{n+1/2,(k)} + \mathbf{R}(\mathbf{u}) \quad (22)$$

where we take the advective term to be piecewise constant in time—this makes the system an ODE system, and can be solved using a standard ODE integrator. Since $[\mathcal{A}(\mathbf{u})]^{n+1/2,(k)}$ is time-centered, this is second-order accurate as long as we use a high-order integrator for the reaction ODE system.

In practice, we only need to evolve the subsystem

$$\mathbf{u}' = (\rho X_k, \rho \alpha_l, \rho \epsilon)^\top \quad (23)$$

and integrate

$$\frac{d\mathbf{U}'}{dt} = [\mathcal{A}(\mathbf{U}')]^{n+1/2,(k)} + \mathbf{R}(\mathbf{U}') , \quad (24)$$

since they are the only quantities that depend on reactions. The remaining quantities can simply be updated with the advective term, e.g.,

$$\rho(t) = \rho^n + (t - t^n)[\mathcal{A}(\rho)]^{n+1/2,(k)} \quad (25)$$

Furthermore, when integrating the reaction network directly, outside of NSE, we do not evolve α_l , but instead compute them as needed from the mass fractions. This system is evolved using the VODE ODE integrator (Brown et al. 1989), with the modifications described in Zingale et al. (2022), although several other integrators are available in our Microphysics suite (see, e.g., Johnson et al. 2023).

This integration begins with \mathbf{U}^n and results in $\mathbf{U}^{n+1,(k)}$.

- *Compute the reactive source terms.* Finally, we compute the \mathcal{I} 's that capture the effect of just the reaction sources on the primitive state variables for the next iteration. This takes the form

$$\mathcal{I}_{\mathbf{q}}^{(k)} = \frac{\mathbf{q}^{n+1,(k)} - \mathbf{q}^n}{\Delta t} - [\mathcal{A}(\mathbf{q})]^{n+1/2,(k)} \quad (26)$$

and we detailed how to compute this in Z22. We note that in the current work, this includes a source term for the α_l , $\mathcal{I}_q^{(k)}(\alpha_l)$.

Two iterations are required for second order convergence in time.

3. REACTION NETWORKS AND NUCLEAR STATISTICAL EQUILIBRIUM

Since we are using the auxiliary composition, α_l , to specify the thermodynamics, we included an advection equation for them above. We can derive evolution equations for each of these composition quantities as:

$$\frac{DY_e}{Dt} = \sum_k \frac{Z_k}{A_k} \frac{DX_k}{Dt} = \sum_k \frac{Z_k}{A_k} \dot{\omega}_k \quad (27)$$

$$\frac{D\bar{A}}{Dt} = -\bar{A}^2 \sum_k \frac{1}{A_k} \frac{DX_k}{Dt} = -\bar{A}^2 \sum_k \frac{1}{A_k} \dot{\omega}_k \quad (28)$$

$$\frac{D}{Dt} \left\langle \frac{B}{A} \right\rangle = \sum_k \frac{B_k}{A_k} \frac{DX_k}{Dt} = \sum_k \frac{B_k}{A_k} \dot{\omega}_k \quad (29)$$

For Strang split coupling of hydro and reactions, $\dot{\omega}_k = DX_k/Dt = 0$, when doing the hydro update, and therefore each of these auxiliary quantities, α_l , obeys an advection equation in the hydro part of the advancement:

$$\frac{\partial(\rho\alpha_l)}{\partial t} + \nabla \cdot (\rho\mathbf{U}\alpha_l) = 0 \quad (30)$$

However, in the SDC approach, we will include the $\mathcal{I}_q(\alpha_l)$ term in the prediction of the interface states to the Riemann solver that captures the source term in Eqs. 27–29.

3.1. Reaction Network and NSE

For this study, we use a reaction network with 19 nuclei: ^1H , ^3He , ^4He , ^{12}C , ^{14}N , ^{16}O , ^{20}Ne , ^{24}Mg , ^{28}Si , ^{32}S , ^{36}Ar , ^{40}Ca , ^{44}Ti , ^{48}Cr , ^{52}Fe , ^{54}Fe , ^{56}Ni , protons (from photodisintegration), and neutrons. This is based on the `aprox19` originally described in [Weaver et al. \(1978\)](#). This describes H and He burning well, and builds an alpha-chain consisting of (α, γ) and $(\alpha, p)(p, \gamma)$ reactions up to ^{56}Ni (as the product of Si-burning). The slightly larger `aprox21` network is often used for massive stars, since it includes ^{45}Fe and ^{48}Cr , allowing the network to reach lower Y_e . But it does not include all of the electron/positron captures and decays that will be taking place in the core of the massive star. To account for these, we blend our network with a table of NSE that provides the Y_e evolution in the core. NSE tables have been used for modeling Type Ia supernova, for example in [Townsend et al. \(2007\)](#); [Seitenzahl et al. \(2009\)](#); [Ma et al. \(2013\)](#), with the latter using `Castro` and blending the NSE state with a 7-isotope network using simple Strang-split coupling.

For this work, we generate the NSE table following the approach of [Seitenzahl et al. \(2009\)](#), as implemented in `pynucastro` ([Smith Clark et al. 2022](#)). Our goal with this paper is to describe the framework for coupling NSE and reactions to hydrodynamics in an accurate fashion. In a follow-on work, we will explore how the details of the nuclear physics used with the on-grid network and NSE table affect the simulations. The entire process for generating the NSE table is open, allowing for the table to easily be updated with new rates. By controlling the generation of the table ourselves, we can experiment with more recent weak rate tabulations and create custom mappings to the on-grid nuclei for a more extensive network. An overview of the table generation is given in Appendix A. Similar to other NSE tabulations, our NSE table takes as inputs ρ , T , and Y_e and tabulates \bar{A} , dY_e/dt , and $\langle B/A \rangle$, $(d\langle B/A \rangle/dt)_{\text{weak}}$, and $\epsilon_{\nu, \text{weak}}$, where the “weak” subscript indicates that these terms are due to the weak rate evolution of the NSE state. By storing dY_e/dt , $(d\langle B/A \rangle/dt)_{\text{weak}}$, and the weak rate neutrino energy loss, $\epsilon_{\nu, \text{weak}}$, we are able to capture the evolution of the NSE state due to electron/positron captures and decays over a timestep. We note that $(d\bar{A}/dt)_{\text{weak}}$ is very small, so we do not consider it.

In our simulations, we carry all 19 isotopes in the main network in each zone and advect them in the hydrodynamics portion of the algorithm. The composition of the larger NSE table is mapped into the 19 isotopes we carry which are also stored on the table. We’ll refer to this reduced composition as \tilde{X}_k . Because the NSE table uses many more nuclei, these approximate \tilde{X}_k do not satisfy Eqs. 3 to 5 directly. This is why we need to explicitly carry the α_l on the grid and evolve them in the hydrodynamics system.

Overall, the NSE function takes the form:

$$\text{nse_table}(\rho, T, Y_e) \rightarrow \bar{A}, \tilde{X}_k, \left\langle \frac{B}{A} \right\rangle, \frac{dY_e}{dt}, \left[\frac{d\langle B/A \rangle}{dt} \right]_{\text{weak}}, \epsilon_{\nu, \text{weak}} \quad (31)$$

We found that to get second-order convergence, we need to use tricubic interpolation, and use a rather dense spacing in (ρ, T, Y_e) . It also helps to store $\langle B/A \rangle$ with enough precision that roundoff error does not pollute the energy generation. Ultimately, the accuracy with which nuclear masses are measured experimentally may limit the convergence.

Our equation of state needs the mean charge per nucleus, \bar{Z} , in addition to the auxiliary quantities, which is computed as

$$\bar{Z} = \bar{A} \sum_k \frac{Z_k X_k}{A_k} = \bar{A} Y_e \quad (32)$$

(see, e.g., [Fryxell et al. 2000](#)).

3.1.1. Initialization

For any problem setup, we need to initial the α_l . We first initialize the mass fractions, X_k , and Y_e , by mapping from a one-dimensional initial model (or using a simple analytic expression for test problems). If Y_e is not available, then we compute Y_e using (3). For the two other composition quantities we carry, \bar{A} , and $\langle B/A \rangle$, we need values that are consistent with the value of Y_e and the nuclei stored in the NSE table. Therefore, if the thermodynamic conditions put us in NSE (using the conditions defined below), then we obtain \bar{A} and $\langle B/A \rangle$ from the NSE table, and use the corresponding \tilde{X}_k instead of the X_k from the initial model. Otherwise, we compute these directly from X_k using (4) and (5).

3.2. NSE condition

For each zone, we need to be able to determine if we are in NSE. Since we integrate energy during the reactions we may begin a zone update out of NSE but enter NSE in the middle of a timestep as the temperature rises. We will address this possibility in the next section. Since we don't have the capability to evaluate individual rates from the table, we use heuristics to determine if NSE applies. We treat a zone as being in NSE if the density and temperature exceed a threshold and the composition is mainly α and Fe-group nuclei (^{48}Cr , ^{52}Fe , ^{54}Fe , and ^{56}Ni). The full condition is:

$$\rho > \rho_{\text{nse}} \quad (33)$$

$$T > T_{\text{nse}} \quad (34)$$

$$X(^4\text{He}) + \sum_{k \in \text{Fe-group}} X_k > A_{\text{nse}} \quad (35)$$

$$X(^{28}\text{Si}) < B_{\text{nse}} \quad (36)$$

Typical values are $\rho_{\text{nse}} = 10^7 \text{ g cm}^{-3}$, $T_{\text{nse}} = 3 \times 10^9 \text{ K}$, $A_{\text{nse}} = 0.88$, and $B_{\text{nse}} = 0.02$. The value of B_{nse} ensures that Si-burning has largely ended before invoking the table. The value of A_{nse} is based on Ma et al. (2013) but our B_{nse} is slightly larger due to the table differences—we need to make sure we are above the maximum amount of ^{28}Si that the NSE state will have (which is $\tilde{X}(^{28}\text{Si}) = 0.012$ for our table).

4. COUPLING NSE WITH REACTION NETWORKS AND HYDRODYNAMICS

We now discuss how to couple hydrodynamics and reactions that potentially enter NSE using the simplified-SDC method. For our reactions, there are 3 parts to the energy generation:

$$\epsilon = \epsilon_{\text{nuc}} - \epsilon_{\nu} - \epsilon_{\nu, \text{weak}} \quad (37)$$

Here ϵ_{nuc} is the energy generation from the nuclear reactions, ϵ_{ν} is the sum of the plasma, photo-, pair-, recombination, and Bremsstrahlung neutrino losses computed via Itoh et al. (1996), and, when using the NSE table, $\epsilon_{\nu, \text{weak}}$ are the neutrino losses from electron-captures and beta-decays (and their positron equivalents). Each of these terms needs to be dealt with separately.

When integrating the network directly, we evolve an energy equation of the form:

$$\frac{d(\rho e)}{dt} = -[\mathcal{A}(\rho e)]^{n+1/2, (k)} + \rho \epsilon_{\text{nuc}} - \rho \epsilon_{\nu} \quad (38)$$

calling the equation of state to get the temperature each time it is needed and evaluating the rates using the `aprox19` network, with no contribution from $\epsilon_{\nu, \text{weak}}$. We then compute ϵ_{nuc} from the change in mass:

$$\epsilon_{\text{nuc}} = -N_A c^2 \sum_k \frac{dY_k}{dt} m_k \quad (39)$$

(see, e.g., [Hix & Meyer 2006](#)) where $Y_k = X_k/A_k$ are the molar fractions of the species and m_k are the nuclei masses, defined as:

$$m_k = (A_k - Z_k)m_n + Z_k(m_p + m_e) - B_k/c^2 \quad (40)$$

where m_n is the neutron mass, m_p is the proton mass, and m_e is the electron mass.

When using the NSE table, we carry the average binding energy per nucleon, so we compute the energy release as:

$$\epsilon_{\text{nuc}} = N_A \frac{d\langle B/A \rangle}{dt} + N_A \Delta m_{np} c^2 \frac{dY_e}{dt} \quad (41)$$

where $\Delta m_{np} = m_n - (m_p + m_e)$ and N_A is Avogadro's number and the second term captures the energy release from weak interactions. This expression is consistent with that shown in [Townesley et al. \(2007\)](#); [Seitenzahl et al. \(2009\)](#).

4.1. SDC-NSE Coupling

With SDC evolution, when we are in NSE, we need to do the advective and reactive updates together. A second-order accurate update takes the form:

$$\mathbf{u}^{n+1,(k)} = \mathbf{u}^n + \Delta t [\mathcal{A}(\mathbf{u})]^{n+1/2,(k)} + \Delta t [\mathbf{R}(\mathbf{u})]^{n+1/2,(k)} \quad (42)$$

For density and momentum, we can do this update already, since there are no reactive sources. That gives us $\rho^{n+1,(k)}$ and $(\rho u)^{n+1,(k)}$. For the other quantities, we do an update based on second-order Runge-Kutta.

Care needs to be taken with regards to the binding energy. We come into the NSE update with a current value for $[\rho \langle B/A \rangle]^n$. If we were already in NSE at the end of the previous timestep, then this should be the same average binding energy of the fluid element as the NSE table would give. But if we are coming from a zone that was previously not in NSE (either at the last timestep or because we bailed out of the current step's integration early) then this $\langle B/A \rangle$ is not consistent with NSE. This means that there are 2 contributions to the energy release during the NSE update: the energy resulting from the change in $\langle B/A \rangle$ from instantaneously converting the input state to NSE and the energy resulting from the evolution of the NSE state over Δt due to weak reactions and the advective changes in the fluid state. As long as we use the incoming $\langle B/A \rangle$ as the starting point and ensure that $\langle B/A \rangle$ on leaving is consistent with the NSE table, we capture both effects.

4.2. EOS Consistency

An additional subtlety comes into play when we try to invert the equation of state to get temperature from energy, since in NSE, the composition depends on temperature. For our equation of state, we have:

$$e = e(\rho, T, \bar{A}, \bar{Z}) \quad (43)$$

but the NSE requirement means \bar{A} and \bar{Z} are also functions of the state, so we write this as:

$$e = e^{\text{NSE}}(\rho, T, \bar{A}(\rho, T, Y_e), \bar{Z}(\rho, T, Y_e)) \quad (44)$$

We'll define the procedure of finding a temperature consistent with the EOS and NSE as `nse_eos`:

$$\text{nse_eos}(\rho, e, Y_e) \rightarrow T, \bar{A} \quad (45)$$

Given an energy, e^* , the EOS procedure is:

- Pick a guess T_0 for the temperature.
- Use the NSE table with T_0 to get \bar{A} and $\bar{Z} = Y_e \bar{A}$.
- Define the function we will zero:

$$f(T) = e^{\text{NSE}}(\rho, T, \bar{A}, \bar{Z}) - e^* \quad (46)$$

with ρ and Y_e held constant.

- Define the correction via Newton-Raphson iteration as:

$$\delta T = -\frac{f(T_0)}{df/dT|_{T_0}} \quad (47)$$

with

$$\left. \frac{\partial f}{\partial T} \right|_{T_0} = \left. \frac{\partial e}{\partial T} \right|_{\rho, \bar{A}, \bar{Z}} + \left(\left. \frac{\partial e}{\partial \bar{A}} \right|_{\rho, T, \bar{Z}} + Y_e \left. \frac{\partial e}{\partial \bar{Z}} \right|_{\rho, T, \bar{A}} \right) \left. \frac{\partial \bar{A}}{\partial T} \right|_{\rho, Y_e} \quad (48)$$

where we used $\bar{Z} = Y_e \bar{A}$. We compute $\partial \bar{A} / \partial T|_{\rho, Y_e}$ by differentiating the cubic interpolant used with the NSE table.

- Correct the initial guess, $T_0 \leftarrow T_0 + \delta T$.
- Iterate until $|\delta T|/T_0$ is small (we use a tolerance of 10^{-6}).

This yields the T and \bar{A} consistent with e^* .

4.3. Integration Algorithm

Since the NSE table gives us the instantaneous values of the state, we start by defining a procedure, `nse_derivs`, to estimate the time derivative of the NSE state, including the evolution due to advection:

$$\text{nse_derivs}(\rho^s, (\rho e)^s, (\rho \alpha_l)^s) \rightarrow [\mathbf{R}(\mathbf{U}')]^s \quad (49)$$

where the time-level of the state, s , is $n \leq s \leq n+1$. `nse_derivs` proceeds as:

- *Compute the initial temperature.*

$$\text{nse_eos}(\rho^s, e^s, (Y_e)^s) \rightarrow T^s, \bar{A}^s \quad (50)$$

where $e^s = (\rho e)^s / \rho^s$ and $(Y_e)^s = (\rho Y_e)^s / \rho^s$.

- *Compute the plasma neutrino losses.*

$$\epsilon_\nu^s = \epsilon_\nu(\rho^s, T^s, \bar{A}^s, \bar{Z}^s) \quad (51)$$

with $\bar{Z}^s = \bar{A}^s \cdot (Y_e)^s$ and $\bar{A}^s = (\rho \bar{A})^s / \rho^s$ from the incoming $(\rho \alpha_l)^s$.

- *Evaluate the NSE state.* This uses the initial thermodynamic state.

$$\text{nse_table}(\rho^s, T^s, (Y_e)^s) \rightarrow \bar{A}^s, (\tilde{X}_k)^s \left\langle \frac{B}{A} \right\rangle^s, \left[\frac{dY_e}{dt} \right]^s, \left[\frac{d\langle B/A \rangle}{dt} \right]_{\text{weak}}^s, \epsilon_{\nu, \text{weak}}^s \quad (52)$$

- *Construct the initial guess of $[\mathbf{R}(\mathcal{U})]^s$.* Since we start out in NSE, this uses only the weak rate evolution and plasma losses:

$$R^*(\rho e) = N_A \rho^s \left[\frac{d\langle B/A \rangle}{dt} \right]_{\text{weak}}^s + N_A \Delta m_{np} c^2 \rho^s \left[\frac{dY_e}{dt} \right]^s - \rho^s (\epsilon_\nu^s + \epsilon_{\nu, \text{weak}}^s) \quad (53)$$

$$R^*(\rho Y_e) = \rho^s \left[\frac{dY_e}{dt} \right]^s \quad (54)$$

$$R^*(\rho \bar{A}) = 0 \quad (55)$$

$$R^*(\rho \langle B/A \rangle) = \rho^s \left[\frac{d\langle B/A \rangle}{dt} \right]_{\text{weak}}^s \quad (56)$$

- *Evolve for a small amount of time τ .* We pick a $\tau \ll \Delta t$ to compute the finite-difference approximation to the derivatives. We'll label this new state with the superscript τ :

$$\mathcal{U}'^{\tau} = \mathcal{U}'^{n} + \tau [\mathcal{A}(\mathcal{U}')]^{n+1/2} + \tau [\mathbf{R}(\mathcal{U}')]^* \quad (57)$$

- *Compute the updated temperature.*

$$\text{nse_eos}(\rho^\tau, e^\tau, Y_e^\tau) \rightarrow T^\tau, \bar{A}^\tau \quad (58)$$

- *Evaluate the new NSE state.* Now we use the thermodynamics state at time τ :

$$\text{nse_table}(\rho^\tau, T^\tau, (Y_e)^\tau) \rightarrow \bar{A}^\tau, (\tilde{X}_k)^\tau, \left\langle \frac{B}{A} \right\rangle^\tau, \left[\frac{dY_e}{dt} \right]^\tau, \left[\frac{d\langle B/A \rangle}{dt} \right]_{\text{weak}}^\tau, \epsilon_{\nu, \text{weak}}^\tau \quad (59)$$

It's important to note that the quantities \bar{A}^τ , $(\tilde{X}_k)^\tau$ and $\langle B/A \rangle^\tau$ returned from the NSE table have implicitly seen the effects of advection.

- *Construct a finite-difference approximation to the reactive sources.* This should not include the advective contribution, so we will need to remove that. We start by defining

$$\widetilde{\rho \left\langle \frac{B}{A} \right\rangle} = \left[\rho \left\langle \frac{B}{A} \right\rangle \right]^\tau - \tau \left[\mathcal{A} \left(\rho \left\langle \frac{B}{A} \right\rangle \right) \right]^{n+1/2, (k)} \quad (60)$$

and

$$\widetilde{\rho \bar{A}} = (\rho \bar{A})^\tau - \tau [\mathcal{A}(\rho \bar{A})]^{n+1/2, (k)} \quad (61)$$

which removes the advective part of the update. Then we define:

$$\Delta \left(\rho \left\langle \frac{B}{A} \right\rangle \right) = \widetilde{\rho \left\langle \frac{B}{A} \right\rangle} - \rho^s \left[\left\langle \frac{B}{A} \right\rangle \right]^* \quad (62)$$

$$\Delta(\rho \bar{A}) = \widetilde{\rho \bar{A}} - \rho^s (\bar{A})^* \quad (63)$$

as the change just due to the NSE evolution of the state over τ . We then compute the sources as:

$$R^s(\rho e) = N_A \frac{\Delta(\rho \langle B/A \rangle)}{\tau} + N_A \Delta m_{np} c^2 \rho^s \left[\frac{dY_e}{dt} \right]^s - \rho^s (\epsilon_\nu^s + \epsilon_{\nu, \text{weak}}^s) \quad (64)$$

$$R^s(\rho Y_e) = \rho^s (dY_e/dt)^s \quad (65)$$

$$R^s(\rho \bar{A}) = \frac{\Delta(\rho \bar{A})}{\tau} \quad (66)$$

$$R^s(\rho \langle B/A \rangle) = \frac{\Delta(\rho \langle B/A \rangle)}{\tau} \quad (67)$$

We note that we don't need the sources for \tilde{X}_k .

This completes the estimation of the reactive sources. A typical value of τ is $\tau = \Delta t/20$.

We can now do the update. We start with the state \mathcal{U}'^n , and compute the derivatives:

$$\text{nse_derivs}(\rho^n, (\rho e)^n, (\rho \alpha_l)^n) \rightarrow [\mathbf{R}(\mathcal{U}')]^n \quad (68)$$

We then predict the state at the midpoint in time:

$$\mathcal{U}'^{n+1/2} = \mathcal{U}'^n + \frac{\Delta t}{2} [\mathcal{A}(\mathcal{U}')]^{n+1/2} + \frac{\Delta t}{2} [\mathbf{R}(\mathcal{U}')]^n \quad (69)$$

Next, we compute the derivatives at the midpoint:

$$\text{nse_derivs}(\rho^{n+1/2}, (\rho e)^{n+1/2}, (\rho \alpha_l)^{n+1/2}) \rightarrow [\mathbf{R}(\mathcal{U}')]^{n+1/2} \quad (70)$$

and finally do the final update:

$$\mathcal{U}'^{n+1} = \mathcal{U}'^n + \Delta t [\mathcal{A}(\mathcal{U}')]^{n+1/2} + \Delta t [\mathbf{R}(\mathcal{U}')]^{n+1/2} \quad (71)$$

With the update complete, we need to compute the new mass fractions and also ensure that $\langle B/A \rangle$ is consistent with the current thermodynamic state, so the next call will not generate energy if $\Delta t \rightarrow 0$. Since the equation of state does not depend on $\langle B/A \rangle$, we start by computing the updated temperature:

$$\text{nse_eos}(\rho^{n+1}, e^{n+1}, Y_e^{n+1}) \rightarrow T^{n+1}, \bar{A}^{n+1} \quad (72)$$

We then call the NSE table:

$$\text{nse_table}(\rho^{n+1}, T^{n+1}, (Y_e)^{n+1}) \rightarrow \bar{A}^{n+1}, (\tilde{X}_k)^{n+1}, \left\langle \frac{B}{A} \right\rangle^{n+1}, \left[\frac{dY_e}{dt} \right]^{n+1}, \left[\frac{d\langle B/A \rangle}{dt} \right]_{\text{weak}}^{n+1}, \epsilon_{\nu, \text{weak}}^{n+1} \quad (73)$$

where, as indicated, we update $\langle B/A \rangle$, \bar{A} and \tilde{X}_k .

The last piece is to update the total energy, which is not part of \mathcal{U}' . This requires the energy source term, which we get from the internal energy:

$$(\rho e)^{n+1/2} = \frac{(\rho e)^{n+1} - (\rho e)^n}{\Delta t} - [\mathcal{A}(\rho e)]^{n+1/2} \quad (74)$$

and then

$$(\rho E)^{n+1, (k)} = (\rho E)^n + \Delta t [\mathcal{A}(\rho E)]^{n+1/2} + \Delta t (\rho e)^{n+1/2} \quad (75)$$

This completes the update.

4.4. NSE Bailout

Because ρ and T evolve during the reactions, it is possible for a zone to start out not in NSE but evolve into NSE during the reaction update. When this happens, the ODE integrator may fail, because an excessive number of timesteps is required. To account for this during the integration, we check to see if zone evolved into NSE, and if so, we finish the zone update using the NSE prescription. To ensure that this is not triggered at the very start of integration, we require a minimum number of steps (10) to have elapsed before checking for NSE. After we leave the integrator, the state is returned to the burner driver where we finish the integration via NSE if the conditions satisfy the NSE criteria. We optionally apply a relaxation factor, typically, 0.9, to the NSE conditions to allow a state that is close to NSE after an integrator failure to enter NSE. If a burn doesn't enter NSE but still fails, then we trigger the **Castro** retry mechanism and throw away the entire timestep and start over with a smaller Δt .

5. NUMERICAL TESTS

5.1. NSE convergence test problem

To test the coupling of the NSE table to the hydrodynamics, we run a similar convergence test to that used in [Zingale et al. \(2019\)](#) and Z22 (and originally inspired by the tests in [McCorquodale & Colella 2011](#)), except with the thermodynamic conditions appropriate for the matter to be in NSE. Additionally, we add a uniform velocity field to ensure that the advective terms have an influence on the update—this exercises the removal of the advective term done in Eqs. 60 and 61. The initial conditions are:

$$\rho = \rho_0 \tag{76}$$

$$T = \begin{cases} T_0 \left[1 + (\delta T) e^{-(r/\lambda)^2} \cos^6(\pi r/L) \right] & r < r_0 \\ T_0 & r \geq r_0 \end{cases} \tag{77}$$

$$Y_e = \begin{cases} (Y_e)_0 \left[1 + (\delta Y_e) e^{-(r/\lambda)^2} \cos^6(\pi r/L) \right] & r < r_0 \\ (Y_e)_0 & r \geq r_0 \end{cases} \tag{78}$$

$$u = u_0 \tag{79}$$

$$v = v_0 \tag{80}$$

where r is the distance from the center of the domain, L is the size of the domain, $r_0 = L/2$, u_0 and v_0 are the initial x - and y -velocities. The value for each parameter is given in Table 1. We chose initial velocity values that keep the motion subsonic so the hydrodynamic slope limiters will not impact the convergence rate much. The peak Mach number initially is $\mathcal{M} = 0.17$. Our initial conditions have Y_e varying between $[0.475, 0.5]$ initially. The mass fractions and remaining composition variables are then initialized from the NSE table.

The domain has a size $[0, L]^2$, and the timestep is fixed as:

$$\Delta t = 4 \times 10^{-4} \left(\frac{32}{N} \right) \text{ s} \tag{81}$$

where N is the number of zones in each direction. We run for 0.032 s with $N = 32, 64, 128, 256$, and 512 zones.

Table 2 shows the convergence. We see that we get close to second order convergence for the lower resolution runs. At higher resolution, the size of the NSE table seems to be the main factor affecting

Table 1. NSE convergence test problem.

parameter	value
ρ_0	$5 \times 10^9 \text{ g cm}^{-3}$
T_0	$5 \times 10^9 \text{ K}$
(δT)	0.2
$(Y_e)_0$	0.5
(δY_e)	-0.05
λ	$2 \times 10^7 \text{ cm}$
L	$2 \times 10^7 \text{ cm}$
u_0	10^8 cm s^{-1}
v_0	10^8 cm s^{-1}

the convergence. This makes sense, since, as we increase the resolution, the truncation error from the hydrodynamics will eventually get smaller than the error from interpolating in the fixed-size table. This test showed us the need for high-order interpolation and a dense NSE table. The conditions for this convergence test are representative of those that we would find in a massive star, and we note that the finest resolution used in the convergence test is 0.39 km, which is much finer than the typical resolution we would use with a star.

5.2. Massive Star

Next we consider the evolution of a massive star, capturing the O and Si burning shells and the evolution of the iron core on the grid.

5.2.1. Initial Model

We use the same $15 M_\odot$ initial model as [Fields & Couch \(2020\)](#), generated by MESA ([Paxton et al. 2011, 2018](#)), representing the state of the star approximately 400 s before collapse (as determined by MESA). The MESA model is interpolated onto a uniform grid and then we reset the composition to the NSE composition if it meets the criteria Eqs. 33–36. We next need to make it consistent with our equation of state and discrete form of hydrostatic equilibrium. This is done by starting at the center and using the model’s T and composition (including Y_e) to find the ρ and p that satisfy HSE (in 1D spherical coordinates) and the EOS. For zone i , this has the form:

$$p_i = p(\rho) = p_{i-1} + \frac{\Delta r}{2}(\rho + \rho_{i-1})g_{i-1/2} \quad (82)$$

where $g_{i-1/2}$ is the gravitational acceleration at the interface between zones $i - 1$ and i in our initial model, computed by adding up all of the mass interior to the interface. We want the pressure p_i , and use Newton-Raphson root finding together with the equation of state to get ρ_i . In the case where we are in NSE, a procedure similar to Eq. 44 and following needs to be done, but now in terms of pressure instead of energy.

Table 2. Convergence (L_1 norm) for the NSE convergence problem using the simplified-SDC algorithm.

field	$\epsilon_{32 \rightarrow 64}$	rate	$\epsilon_{64 \rightarrow 128}$	rate	$\epsilon_{128 \rightarrow 256}$	rate	$\epsilon_{256 \rightarrow 512}$
ρ	2.924×10^{19}	1.990	7.359×10^{18}	1.848	2.044×10^{18}	1.732	6.153×10^{17}
ρu	1.383×10^{28}	1.896	3.714×10^{27}	1.835	1.041×10^{27}	1.741	3.115×10^{26}
ρv	1.383×10^{28}	1.896	3.714×10^{27}	1.835	1.041×10^{27}	1.741	3.115×10^{26}
ρE	3.585×10^{37}	1.870	9.805×10^{36}	1.894	2.639×10^{36}	1.715	8.038×10^{35}
ρe	3.529×10^{37}	1.872	9.638×10^{36}	1.892	2.596×10^{36}	1.713	7.923×10^{35}
T	7.190×10^{20}	2.075	1.706×10^{20}	1.921	4.506×10^{19}	1.908	1.200×10^{19}
$\rho X(^4\text{He})$	2.991×10^{18}	1.999	7.484×10^{17}	1.914	1.986×10^{17}	1.941	5.172×10^{16}
$\rho X(^{48}\text{Cr})$	1.645×10^{19}	2.188	3.609×10^{18}	2.071	8.589×10^{17}	1.987	2.166×10^{17}
$\rho X(^{52}\text{Fe})$	4.621×10^{19}	1.892	1.245×10^{19}	1.849	3.457×10^{18}	1.972	8.814×10^{17}
$\rho X(^{54}\text{Fe})$	4.251×10^{20}	2.230	9.059×10^{19}	2.161	2.026×10^{19}	2.158	4.541×10^{18}
$\rho X(^{56}\text{Ni})$	4.436×10^{20}	2.244	9.365×10^{19}	2.160	2.095×10^{19}	2.129	4.789×10^{18}
$\rho X(\text{n})$	3.835×10^{14}	1.710	1.172×10^{14}	1.792	3.383×10^{13}	2.035	8.254×10^{12}
$\rho X(\text{p})$	8.642×10^{17}	2.232	1.840×10^{17}	1.845	5.121×10^{16}	1.766	1.506×10^{16}
ρY_e	1.686×10^{19}	1.953	4.354×10^{18}	1.873	1.189×10^{18}	1.786	3.448×10^{17}
$\rho \bar{A}$	4.188×10^{21}	2.216	9.013×10^{20}	1.846	2.507×10^{20}	1.646	8.010×10^{19}
$\rho(B/A)$	2.977×10^{20}	1.990	7.493×10^{19}	1.881	2.034×10^{19}	1.794	5.864×10^{18}

We use a 1D spacing of $\Delta r = 5$ km. Figure 1 shows the structure and composition of the initial model. The code to remap the initial model is freely available ([AMReX-Astro initial_models team et al. 2024](#)).

5.2.2. Convective Initialization

We map the initial model onto the Cartesian grid by taking pressure, density, composition, and Y_e as inputs and interpolating them to cell centers. We then check if a cell is in NSE, and if so, we update the composition and $\langle B/A \rangle$ from the NSE table; otherwise, we compute $\langle B/A \rangle$ using the composition in the cell. Finally, we call the EOS to get the temperature. Just like with the initial model, if we are in NSE, then we need to do the EOS inversion self-consistent with the NSE table, analogous to Eq. 44, but using the interpolated p instead of e .

To break the symmetry, a small velocity perturbation is added to the Si layer. We define an amplitude:

$$\gamma_{l,m,n} = c^l a^m b^n (-1)^n \quad (83)$$

and phases as:

$$\phi_{l,m,n}^{(x)} = 2\pi c^l b^m a^n \quad (84)$$

$$\phi_{l,m,n}^{(y)} = 2\pi b^l c^m a^n \quad (85)$$

and a normalization:

$$\eta_{l,m,n} = (l^2 + m^2 + n^2)^{1/2} \quad (86)$$

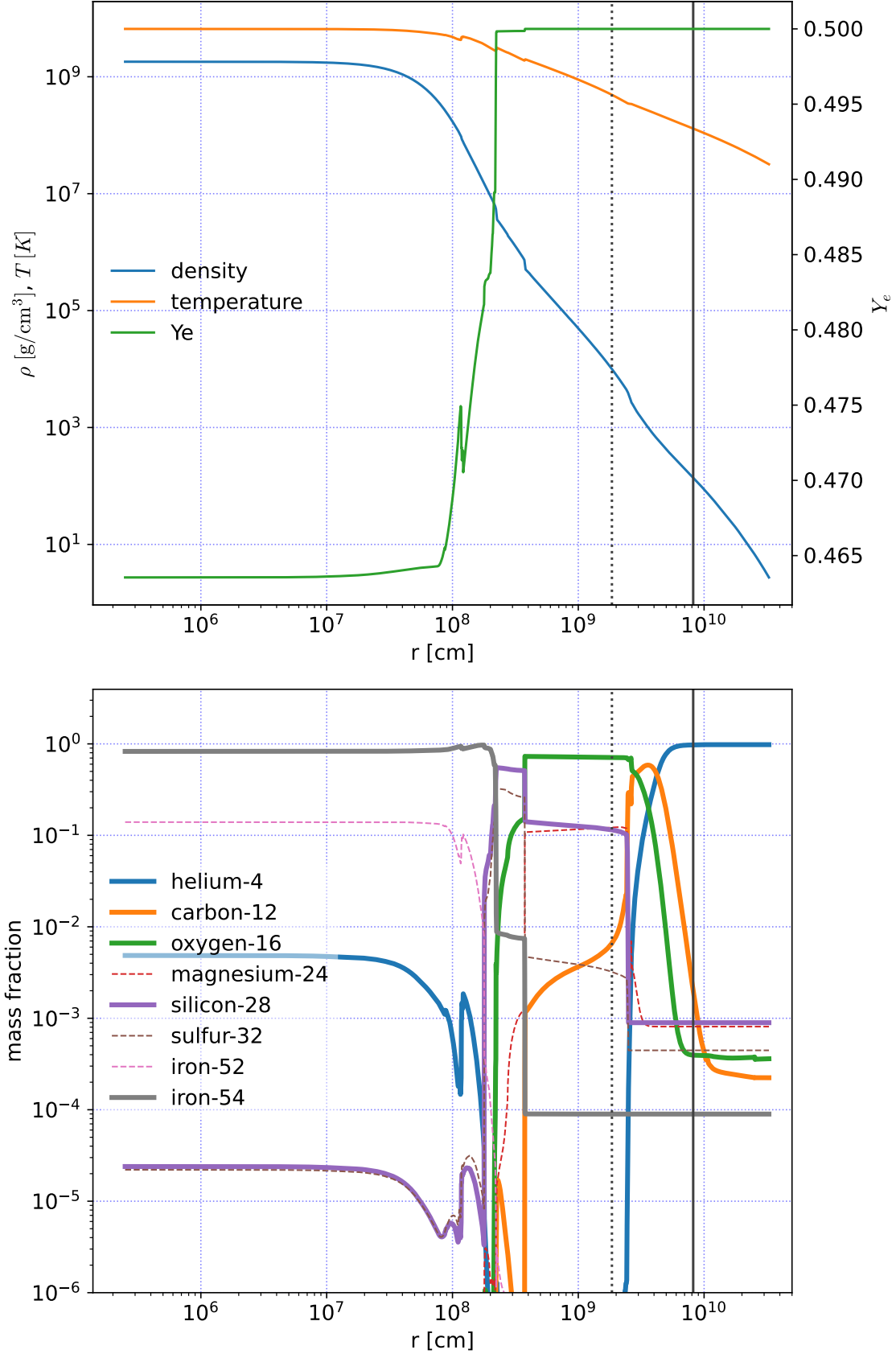


Figure 1. $15M_{\odot}$ initial model showing the structure and composition of the region near the core. The dotted vertical line shows the radius inside of which we refine to higher resolution. The solid vertical line shows the radius corresponding to our domain width.

Then we define the velocity field in x (u) and y (v) as:

$$u_{i,j} = -A_{\text{pert}} X(^{28}\text{Si}) \sum_{l=1}^3 \sum_{m=1}^3 \sum_{n=1}^3 \gamma_{l,m,n} \frac{m}{\eta_{l,m,n}} \cos\left(\frac{2\pi l x_i}{\lambda} + \phi_{l,m,n}^{(x)}\right) \sin\left(\frac{2\pi m y_j}{\lambda} + \phi_{l,m,n}^{(y)}\right) \quad (87)$$

$$v_{i,j} = A_{\text{pert}} X(^{28}\text{Si}) \sum_{l=1}^3 \sum_{m=1}^3 \sum_{n=1}^3 \gamma_{l,m,n} \frac{l}{\eta_{l,m,n}} \sin\left(\frac{2\pi l x_i}{\lambda} + \phi_{l,m,n}^{(x)}\right) \cos\left(\frac{2\pi m y_j}{\lambda} + \phi_{l,m,n}^{(y)}\right) \quad (88)$$

where λ is the characteristic scale of the fluctuations in the velocity field. The factor of $X(^{28}\text{Si})$ ensures that this perturbation is confined to the silicon-burning layer. We take $a = 0.5$, $b = 0.7$, and $c = 0.3$, and $A_{\text{pert}} = 5 \times 10^6 \text{ cm s}^{-1}$, $\lambda = 10^7 \text{ cm}$. The peak Mach number of this initial velocity field is 0.0016.

When mapping from a one-dimensional model that used mixing length theory to a multi-dimensional model, there is not enough information to initialize the velocity field. This means that as soon as the simulation begins, the burning at the base of the convective layer will release lots of energy that is not carried away, resulting in a nonlinear feedback that can cause problems (for example, thermonuclear runaways). To help mitigate this problem, we use a special initialization procedure to help establish a convective field. This is the *drive initial convection* feature in **Castro**. The basic algorithm is:

- Allow star to evolve for a time τ_{reset} . During this time, calls to the nuclear reaction network will use the temperature interpolated from the initial model instead of the temperature on the grid. This breaks the nonlinear runaway that can occur from the burning happening "in-place" since there is no convective field to carry the energy away. Note: the SDC-NSE update, described in section 4.1, differs slightly during this phase, since the temperature is held fixed.
- After the τ_{reset} has elapsed, we reinitialize the initial thermodynamic state (by again mapping directly from the initial model), but leave the velocity field unchanged from what is on the grid.
- We repeat this evolve-remap process every τ_{reset} . This will slowly build up a convective velocity field that respects the initial model.
- After a time τ_{drive} , we stop this initialization process and evolve as normal.

A different solution to this problem was used in the anelastic calculations of core convection in Chandrasekhar mass white dwarfs by [Kuhlen et al. \(2006\)](#), where the energy generation was expressed as a power law in terms of the background temperature, with linear perturbations for the duration of the simulation. That works well for the "simmering" they modeled. In our case, we need to capture the nonlinearity of the reactions, and our method allows for that once the convective field is established. For these simulations, unless otherwise noted, we use $\tau_{\text{reset}} = 2 \text{ s}$ and $\tau_{\text{drive}} = 50 \text{ s}$.

5.2.3. Simulations

We run 7 simulations, each with slightly different parameters to assess the sensitivity of the evolution to the problem setup. Table 3 summarizes the simulations. The default simulation, `ms`, uses a domain that is $8.192 \times 10^9 \text{ cm} \times 1.6384 \times 10^9 \text{ cm}$ in a 2D axisymmetric (r - z) geometry. The base grid is 1024×2048 zones and 2 levels of refinement are used, each jumping by a factor of 2, giving a fine-grid resolution of 20 km. This is slightly less than the 16 km resolution of [Couch et al. \(2015\)](#). Refinement is done by tagging

Table 3. Parameters for our simulation suite.

name	domain size (km)	coarse grid	refinement (num : jumps)	CFL	τ_{drive} (s)	ρ_{sponge} g cm^{-3}	note
ms	8192×16384	1024×2048	2: $2\times, 2\times$	0.4	50	10^3	
ms-100	8192×16384	1024×2048	2: $2\times, 2\times$	0.4	100	10^3	
ms-cfl2	8192×16384	1024×2048	2: $2\times, 2\times$	0.2	50	10^3	
ms-cfl8	8192×16384	1024×2048	2: $2\times, 2\times$	0.8	50	10^3	
ms-sp	12288×24576	768×1536	3: $2\times, 2\times, 2\times$	0.4	50	10^2	
ms-enu	8192×16384	1024×2048	2: $2\times, 2\times$	0.4	50	10^3	includes $\epsilon_{\nu, \text{weak}}$
ms-noburn	8192×16384	1024×2048	2: $2\times, 2\times$	0.4	50	10^3	no pert; no reactions

all cells that have a density larger than 10^4 g cm^{-3} , encompassing most of the O shell. Figure 1 shows the extent of the refined region and the domain. Subcycling is used to advance coarse zones at larger timesteps than fine zones. The gravitational acceleration is computed as a simple monopole, with the source term treated conservatively (as described in Katz et al. 2016). Integration is done with $\text{CFL} = 0.4$, without any reaction-based timestep limiter. Evolving to $t - \tau_{\text{drive}} = 300\text{s}$ takes 98755 coarse timesteps for ms.

The $r = 0$ boundary is reflecting, enforcing the axisymmetric geometry. For the three other boundaries, we use a simple zero-gradient outflow. However, this alone is not sufficient to keep the star stable in hydrostatic equilibrium when there are no reactions. In the work of Chatzopoulos et al. (2016), a diode boundary condition was used—allowing material to exit the domain but not enter. Instead, we use a sponging term to the momentum equation, following the same prescription of Eiden et al. (2020). This turns on at a density of ρ_{sponge} and comes into full effect when the density drops by an order of magnitude. For the ms simulation, we use $\rho_{\text{sponge}} = 10^3 \text{ g cm}^{-3}$. This is outside of the O shell. We’ll explore the effect of this choice in the ms-sp simulation.

The contribution to the energy generation from weak-rate neutrinos, $\epsilon_{\nu, \text{weak}}$, is disabled—as we’ll see shortly, including this term leads to an almost instantaneous collapse, suggesting a mismatch between the weak rate neutrino physics in the MESA model and what we’ve modeled here. Consistency between the nuclear physics used in the 1D model and that used here will be explored in a follow-on paper. The convection is driven for $\tau_{\text{drive}} = 50 \text{ s}$, after which the problem is left to evolve.

All simulations are run on the NERSC Perlmutter machine using 8 nodes, and running completely on the 4 NVIDIA A100 GPUs / node using CUDA through the C++ performance portability framework enabled in AMReX (Zhang et al. 2019). Evolving in 2D for 200 seconds takes about 244 node-hours.

Figures 2–4 show the evolution of the ms simulation in the region close to the core (only 10% of the domain in each dimension is shown). The first panel is immediately after the convective initialization procedure ends. As time evolves, we see well-defined convection in the Si shell, but at the later times, as the convection in the O shell becomes more vigorous, the shell begins to erode. This is likely an effect of the two-dimensional nature of the simulation. Since our focus for this paper is the time-integration algorithm, we do not explore 3D here.

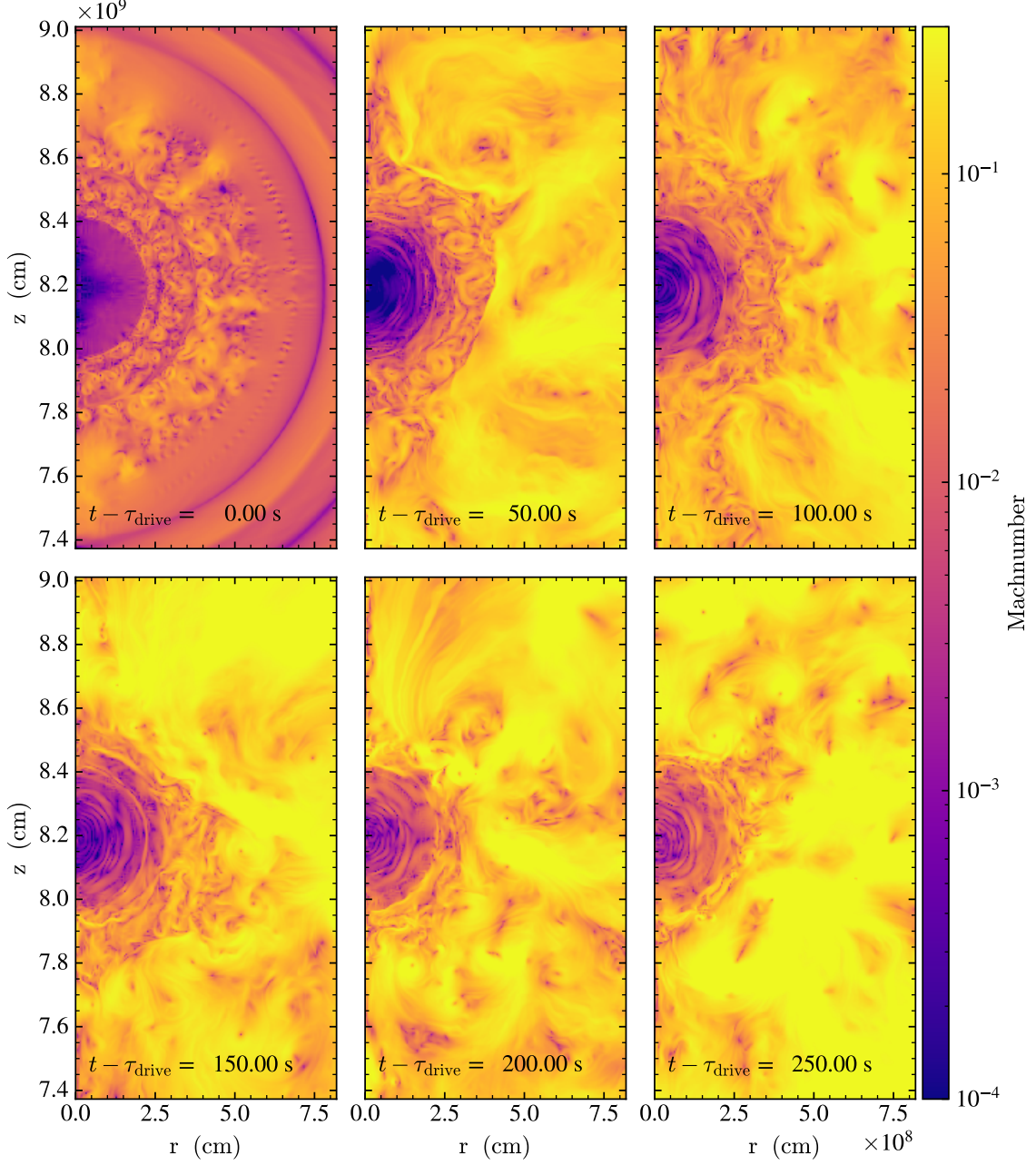


Figure 2. Mach number sequence for the `ms` simulation focusing on the region near the core. The first frame is just after the drive initial convection phase.

Zooming out, Figure 5 shows the state on a much larger scale. Here we clearly see the large scale vortices in the O shell that dominate the flow. We also see that the Mach number can get quite high there. Again, we expect much of this behavior to be an artifact of the 2D geometry.

Next we look at how the integral properties of the simulations differ as we adjust some model parameters. The `ms-100` simulation doubles τ_{drive} from 50 s to 100 s. The `ms-cfl2` and `ms-cfl8` simulations explore CFL numbers of 0.2 and 0.8, respectively. The `ms-sp` simulation uses a domain that is 50% larger (in each dimension) and drops ρ_{sponge} from 10^3 g cm^{-3} to 100 g cm^{-3} —this allows us to understand how

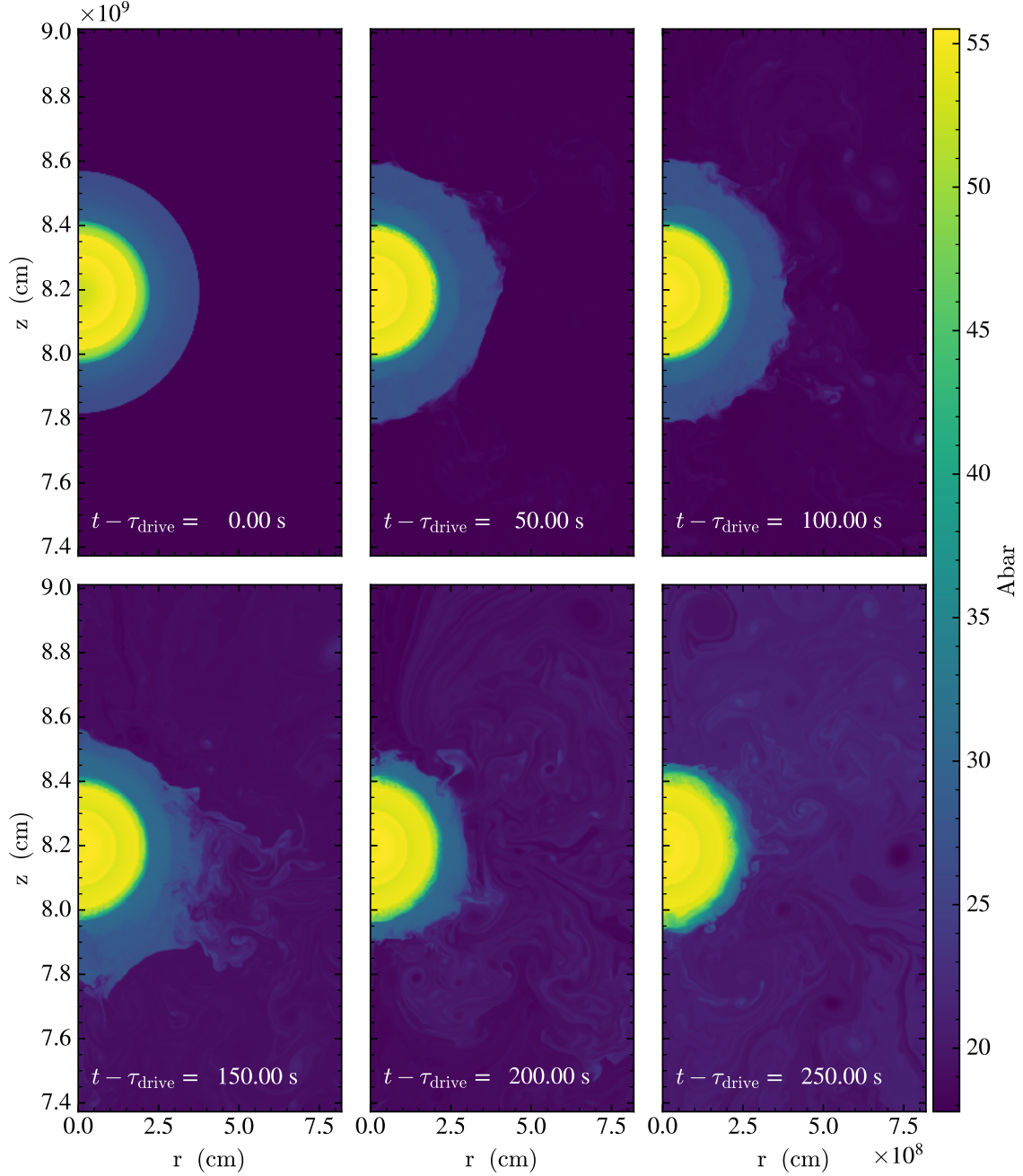


Figure 3. Time sequence of \bar{A} for the ms simulation, focusing on the region near the core.

well our outer boundary works. This also means that the evolution of the full C shell is now captured on the grid. Figure 6 shows the evolution of the maximum density on the grid as a function of time for the different simulations. We see strong agreement between ms, ms-100, ms-cfl2, ms-cfl8, and ms-sp—for each, the central density slowly increases in time, reaches a peak around 150 s, and then begins to decrease. This peak corresponds to the point shown in Figure 3 where the O convection begins to erode the Si layer. Again we note that this is very likely a 2D effect. Figure 7 shows the peak temperature evolution, and we see the same trend for this group of simulations. Figure 8 shows the minimum Y_e on the grid. All simulations show a decrease in time, and none fall below $Y_e = 0.43$, which is the boundary of our table. Finally, Figure 9

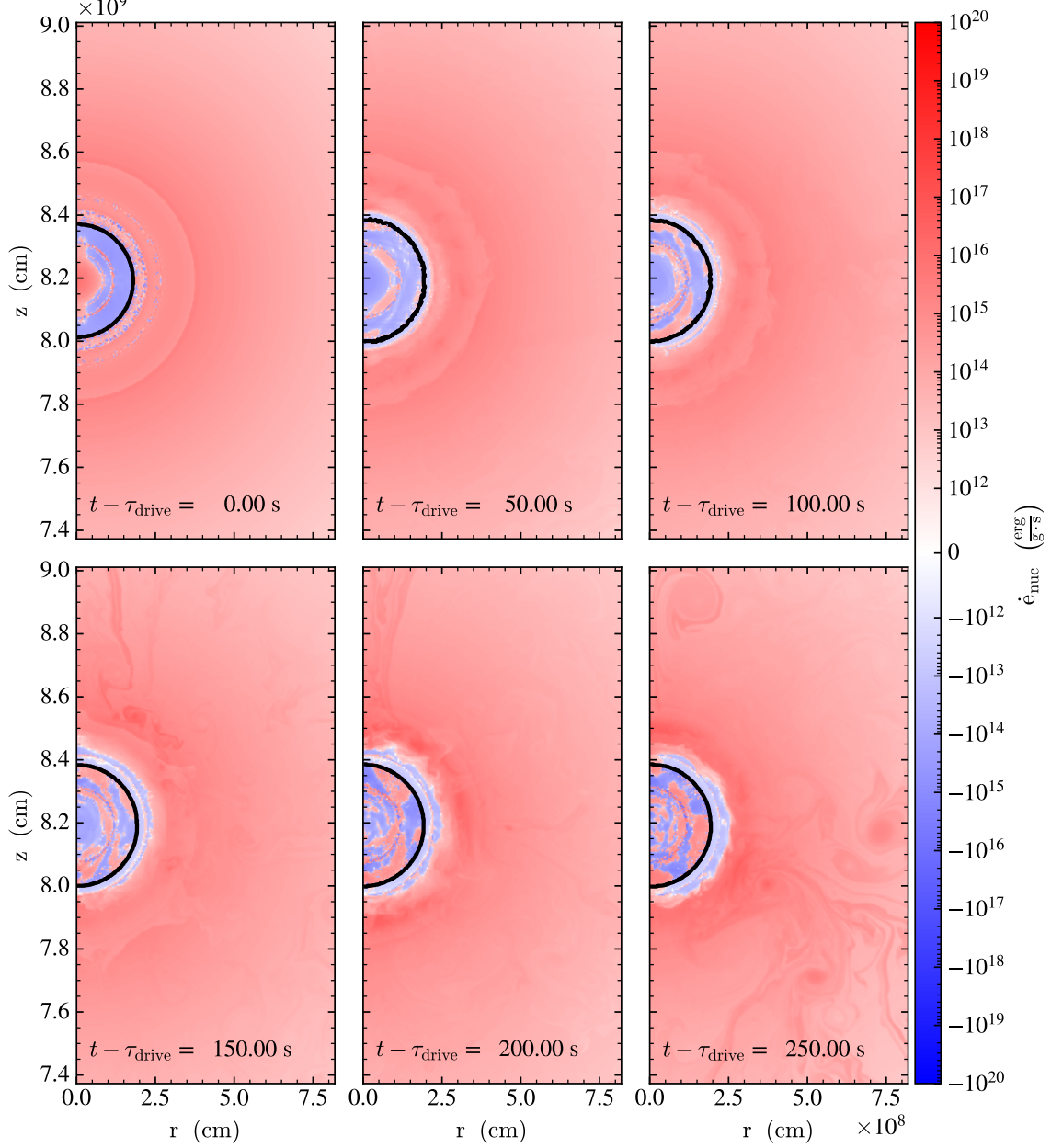


Figure 4. Time sequence of the energy generation rate for the `ms` simulation focusing on the region near the core. The back contour separates the region where the NSE table is used from the region where the full network is integrated.

shows the total mass of ^{28}Si and ^{32}S . We see the mass of these elements decreasing initially, but again, near 150 s, the trend inverts and we begin producing more of these nuclei. This is consistent with the idea that the strong 2D O-shell convection begins disrupting the Si shell, bringing fresh O into hot regions and increases these abundances. The key takeaway from these figures is that our evolution is largely insensitive to the domain size / sponging, CFL, and initialization.

Finally the `ms-enu` simulation enables the $\epsilon_{\nu, \text{weak}}$ term in the energy generation in the NSE region. We see that the density increases dramatically right from the start, leading to a collapse. This suggests that the MESA initial model, which used `aprox21`, did not capture all of these neutrino losses.

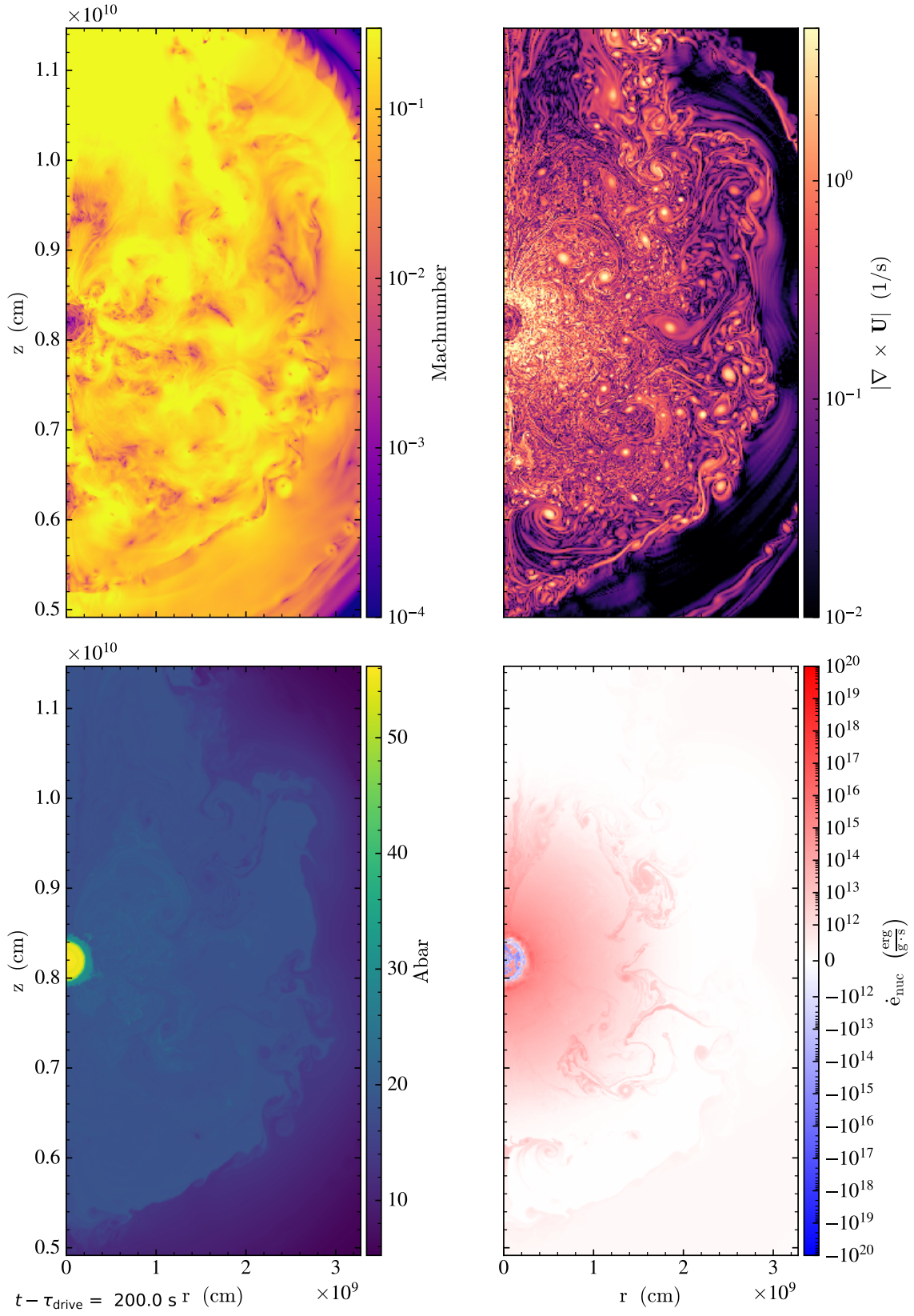


Figure 5. The state of the convection in the m_s simulation in a large region of the star, 200 s after the drive initial convection. The full O shell is seen on this scale.

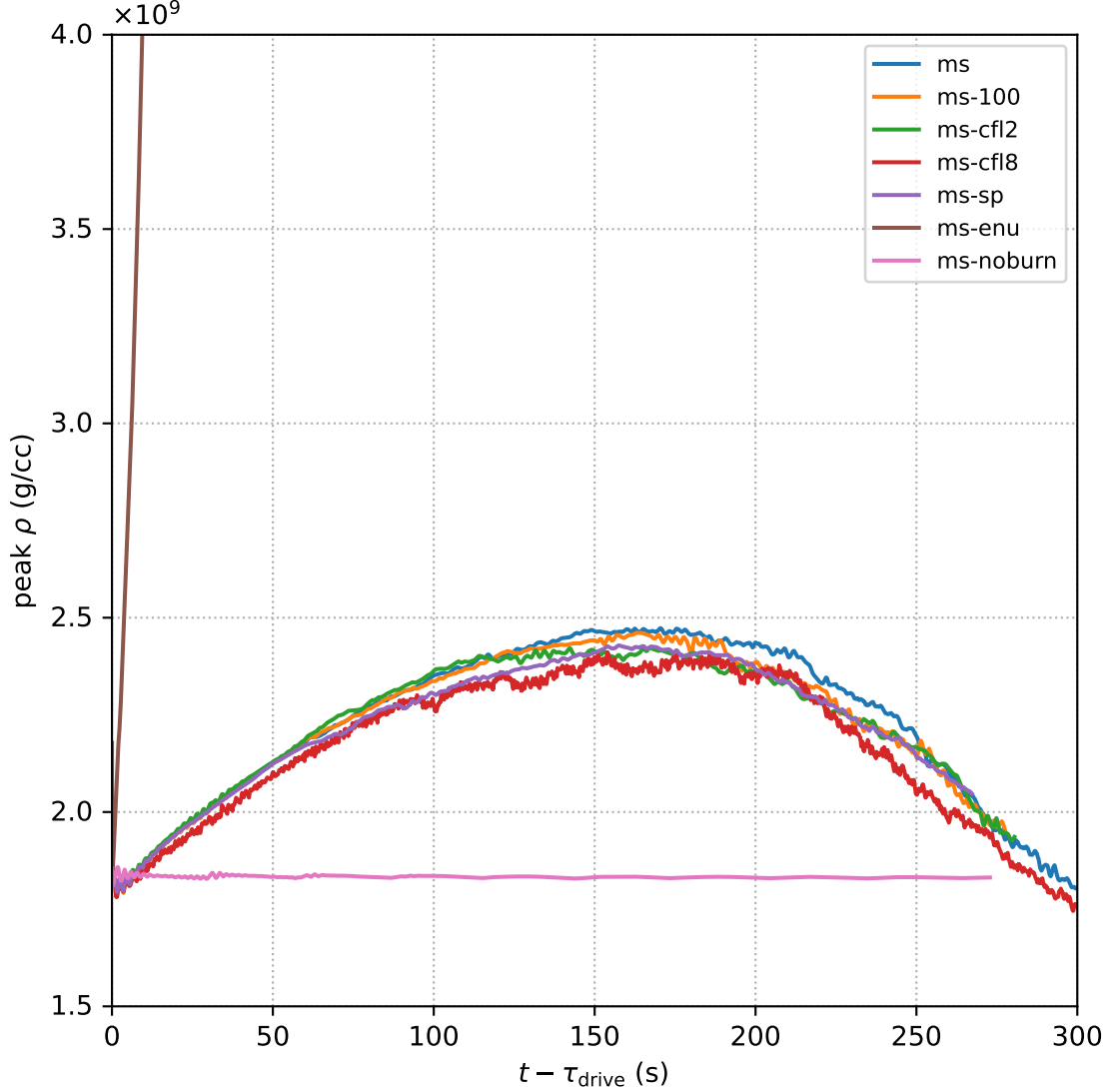


Figure 6. Peak density vs. time since the drive initial convection process ended for the 7 different simulations.

One more simulation is done—`ms-noburn` disables the initial velocity perturbation and turns off all reactions, to serve as a check that the star remains in HSE on our grid for long timescales. As noted in [Mocák et al. \(2010\)](#), the temperature gradient from the initial model can drive convective motions in multi-dimensional simulations, so disabling reactions does not mean no motion on the grid. But the run with `ms-noburn` should not show any largescale structure evolution. We see that the density remains nearly constant in this simulation, showing that our star is stable in the absence of energy generation. Interestingly, if we do this same simulation without the sponge, the star eventually collapses as material flows through the outer boundary. This demonstrates that our treatment of the outer boundary with a sponge is essential.

6. SUMMARY

We presented a simplified spectral deferred corrections scheme for coupling hydrodynamics and reactions when nuclear statistical equilibrium is established. We showed that the method is second-order accurate and

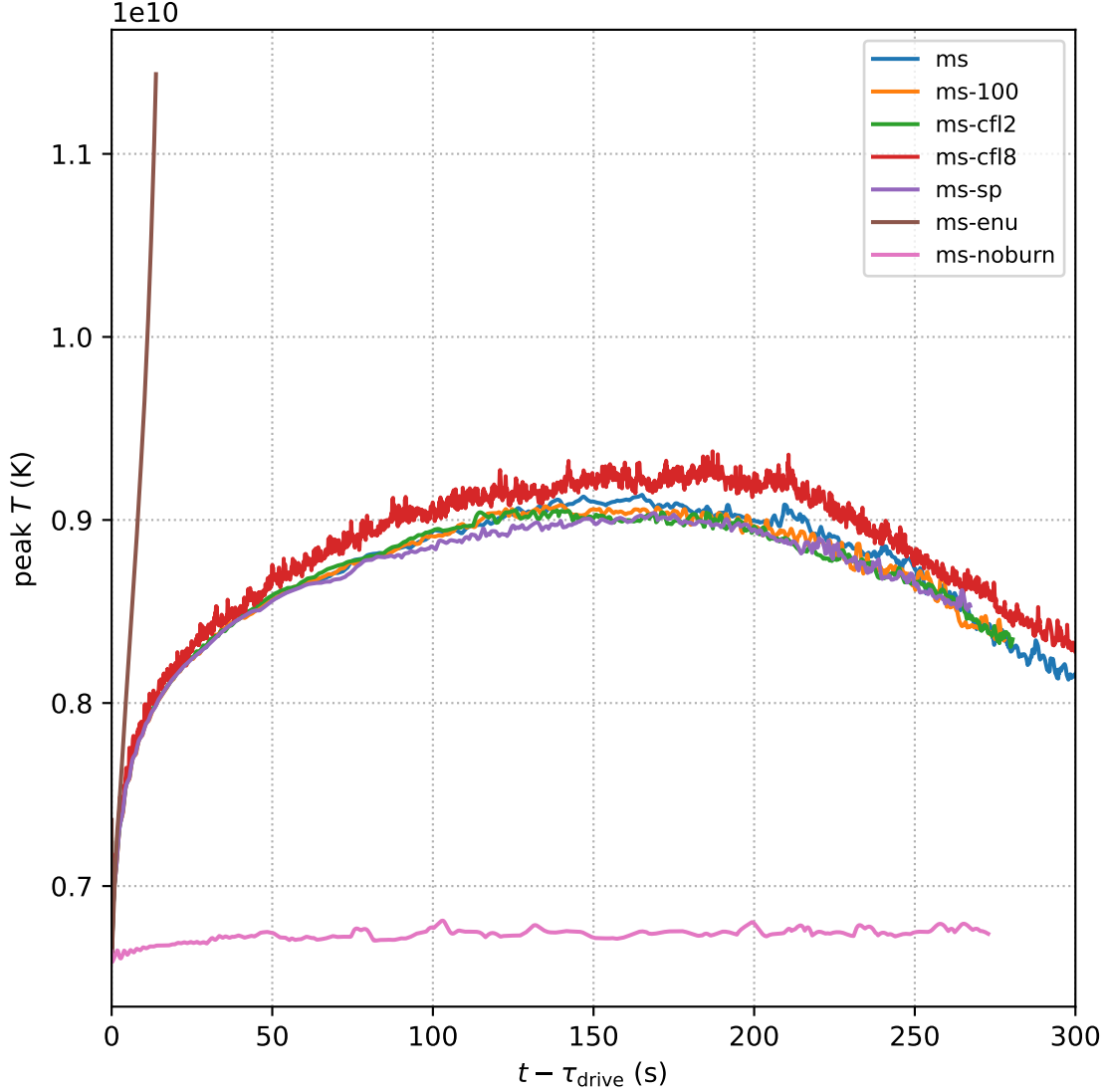


Figure 7. Peak temperature vs. time since the drive initial convection process ended for the 7 different simulations.

provides an effective simulation method for modeling convection in massive stars, including the evolution of the core on the grid. Furthermore, the time-integration algorithm allows for evolution on the hydrodynamics timescale and with GPU acceleration is very efficient on today’s supercomputers. This entire simulation methodology is freely available in the AMReX-Astro github organization¹.

Additionally, a procedure for driving the initial convection was shown to help establish a robust convective field for the initial model. It should be possible to do this at a coarser resolution and then add a refinement level (or more) for the last few τ_{drive} periods to get the benefits of this initialization without a large computational cost.

We will follow this work with a 3D simulation. Currently we are fully refining all regions where the density is greater than 10^4 g cm^{-3} . This corresponds to a radius of about 20,000 km. In Couch et al. (2015),

¹ <https://github.com/AMReX-Astro/>

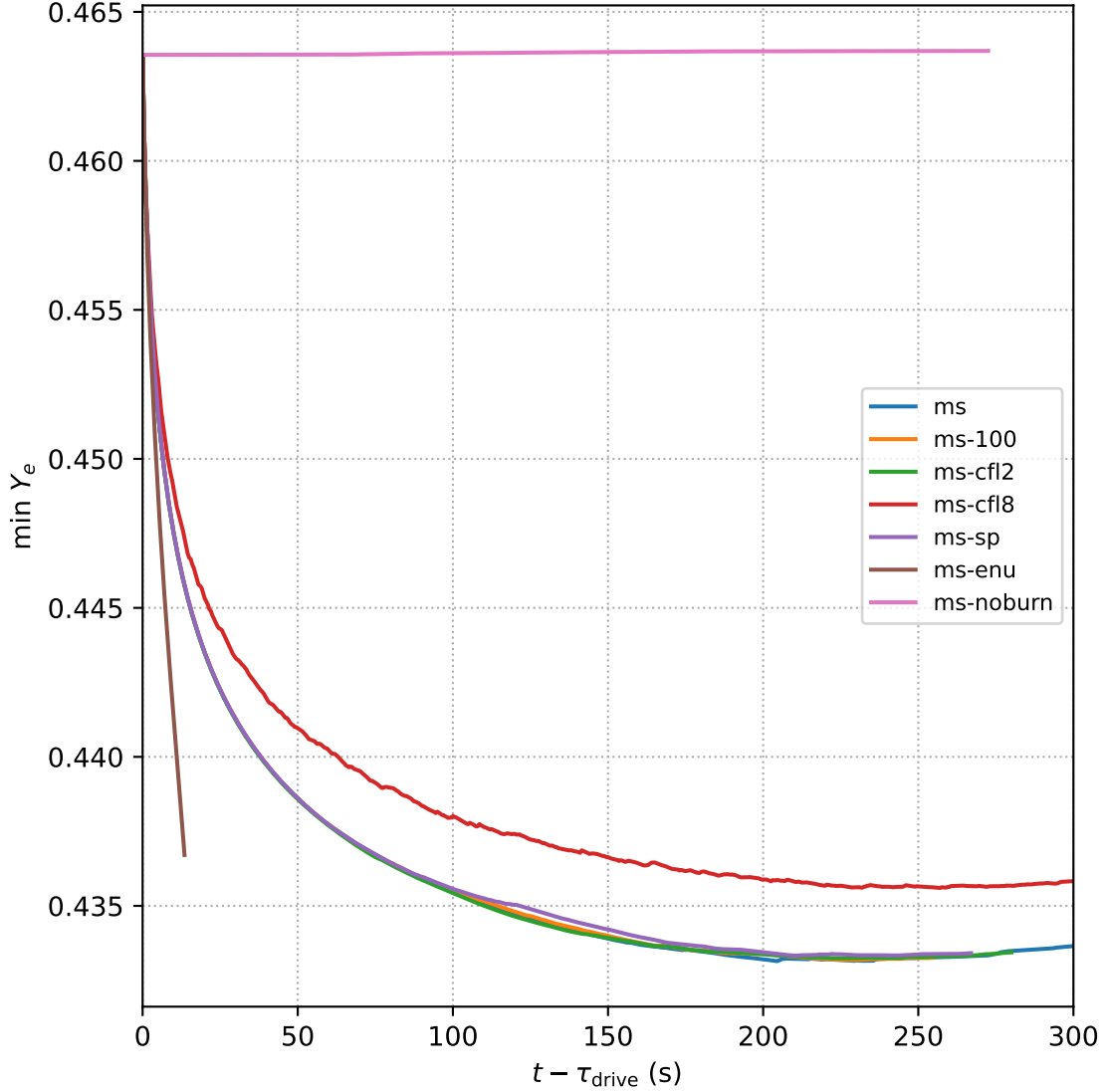


Figure 8. Minimum Y_e vs. time since the drive initial convection process ended for the 7 different simulations.

only the inner 2,500 km was fully refined. To reduce the computational cost for 3D, we will need to relax our refinement with radius compared to the 2D models presented here. Initial estimates show that a 3-level simulation, evolving $\rho > 3 \times 10^5 \text{ g cm}^{-3}$ at 20 km (corresponding to $r < 4700 \text{ km}$), $\rho > 2 \times 10^3 \text{ g cm}^{-3}$ at 80 km, and the base grid at 320 km resolution (each jump is $4\times$) will need approximately 40,000 node hours on the OLCF Frontier machine to evolve for 350 s (including the 50 s of convective initialization). This estimate uses HIP to offload the compute kernels to the AMD Instinct MI250X GPUs, similar to how we use CUDA with NVIDIA GPUs at NERSC. We expect to bring this cost down with further optimization on AMD GPUs.

It is straightforward to adapt this to the case where we compute the NSE abundance from the ongrid network itself instead of using a table. The same time integration algorithm will apply when the entire network is in NSE, which can be detected using the same procedures described, for example, in [Kushnir &](#)

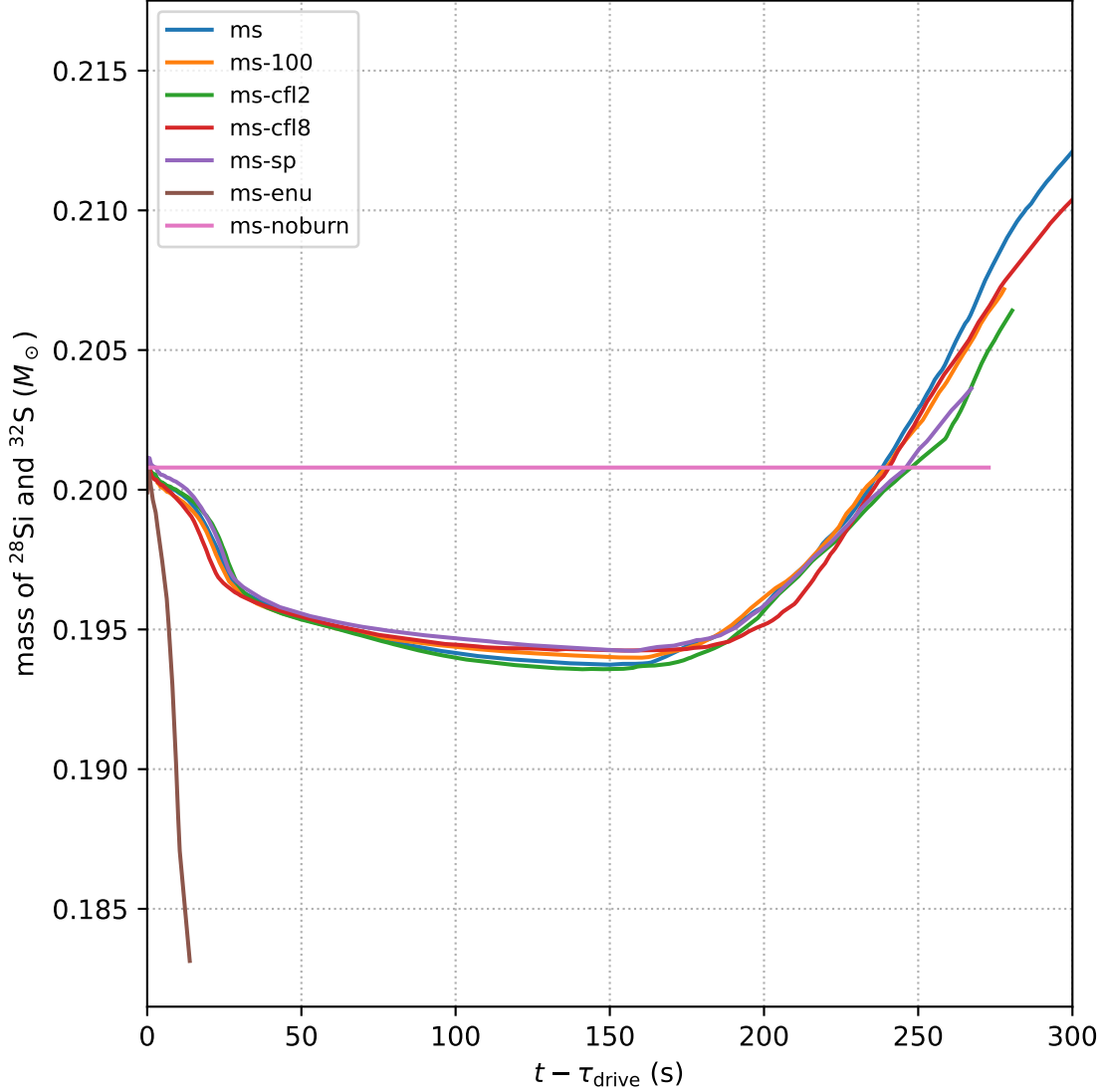


Figure 9. Total ^{28}Si and ^{32}S mass vs. time since the drive initial convection process ended for the 7 different simulations.

Katz (2020). This can be applied to the double detonation model in Type Ia supernovae and benefit from the second-order accuracy demonstrated here.

This same overall integration framework can apply to our low-Mach number stellar hydrodynamics code MAESTROeX (Fan et al. 2019). We will explore this in the future to possibly allow for longer-term evolution beginning at earlier times if we find that the Mach numbers are low enough. This was used previously to model H core convection in massive stars (Gilet et al. 2013). MAESTROeX and Castro share the same AMReX-Astrophysics Microphysics package.

The focus of this paper was the development of an accurate time-integration strategy for convective burning in massive stars. In follow-on work, we will explore the physics of this convective burning and the evolution of different progenitor massive stars. We will also explore how sensitive the numerical results are to our choice of network (both the on-grid network and our NSE tabulations), spatial resolution, and

the details of the initial model. For this new work, we will generate new initial models that start earlier in evolution and explore getting better consistency with the nuclear physics inputs in the stellar evolution code.

ACKNOWLEDGEMENTS

Castro and the AMReX-Astrophysics suite are freely available at <http://github.com/AMReX-Astro/>. All of the code and problem setups used here are available in the git repo: the convergence test is in `Castro/Exec/reacting_tests/nse_test` and the massive star convection problem is in `Castro/Exec/science/massive_star`. The script used to generate the NSE grid is in `Microphysics/nse_tabular`. We thank Carl Fields for sharing the initial model with us. We thank Stan Woosley for helpful discussions about the NSE table used in the work of [Ma et al. \(2013\)](#). The work at Stony Brook was supported by DOE/Office of Nuclear Physics grant DE-FG02-87ER40317. This material is based upon work supported by the U.S. Department of Energy, Office of Science, Office of Advanced Scientific Computing Research and Office of Nuclear Physics, Scientific Discovery through Advanced Computing (SciDAC) program under Award Number DE-SC0017955. This research used resources of the National Energy Research Scientific Computing Center (NERSC), a Department of Energy Office of Science User Facility using NERSC award NP-ERCAP0027167. This research used resources of the Oak Ridge Leadership Computing Facility at the Oak Ridge National Laboratory, which is supported by the Office of Science of the U.S. Department of Energy under Contract No. DE-AC05-00OR22725.

Software: AMReX ([Zhang et al. 2019](#)), Castro ([Almgren et al. 2010](#); [Almgren et al. 2020](#)), GNU Compiler Collection (<https://gcc.gnu.org/>), Linux (<https://www.kernel.org>), matplotlib ([Hunter 2007](#), <http://matplotlib.org/>), NumPy ([Oliphant 2007](#); [van der Walt et al. 2011](#); [Harris et al. 2020](#)), pynucastro ([Willcox & Zingale 2018](#); [Smith Clark et al. 2022](#)), python (<https://www.python.org/>), SciPy ([Jones et al. 2001](#)–; [Virtanen et al. 2020](#)), SymPy ([Meurer et al. 2017](#)), valgrind ([Nethercote & Seward 2007](#)), yt ([Turk et al. 2011](#))

Facilities: NERSC, OLCF

APPENDIX

A. CONSTRUCTING THE NSE TABLE

We use pynucastro ([Willcox & Zingale 2018](#); [Smith Clark et al. 2022](#)) to construct the NSE table, making use of the features in the latest version ([Smith Clark et al. 2023](#)). We use the weak rates from [Langanke & Martínez-Pinedo \(2001\)](#) to be consistent with the work from [Seitenzahl et al. \(2009\)](#); [Ma et al. \(2013\)](#). But by using a completely open, reproducible framework built from pynucastro, we can regenerate the table easily as newer rate compilations are added to pynucastro, for example the those of [Giraud et al. \(2022\)](#). The solution procedure follows that of [Seitenzahl et al. \(2009\)](#), and we note that we assume that the nuclei behave as an ideal gas, consistent with our equation of state and a good approximation for the densities we model here.

Nuclear masses are taken the atomic mass evaluation (AME) 2016 database ([Huang et al. 2017](#); [Wang et al. 2017](#)) and spins from [Kondev et al. \(2021\)](#). The temperature-dependent partition functions come from [Rauscher et al. \(1997\)](#); [Rauscher \(2003\)](#). Finally, we use the Coulomb screening implementation from [Chabrier & Potekhin \(1998\)](#).

We setup a network with 96 nuclei: n, p, d, $^3\text{--}^4\text{He}$, ^{12}C , $^{13\text{--}14}\text{N}$, ^{16}O , ^{18}F , $^{20\text{--}22}\text{Ne}$, ^{23}Na , ^{24}Mg , ^{27}Al , ^{28}Si , ^{31}P , ^{32}S , ^{35}Cl , ^{36}Ar , ^{39}K , $^{40,45\text{--}48}\text{Ca}$, $^{43,45\text{--}49}\text{Sc}$, $^{44\text{--}52}\text{Ti}$, $^{47\text{--}54}\text{V}$, $^{48\text{--}56}\text{Cr}$, $^{51\text{--}58}\text{Mn}$, $^{52\text{--}60}\text{Fe}$, $^{54\text{--}61}\text{Co}$, $^{56\text{--}65}\text{Ni}$, ^{59}Cu , ^{60}Zn . This selection of nuclei is smaller than that of [Ma et al. \(2013\)](#) and [Seitenzahl et al. \(2009\)](#), in part because we are restricting ourselves to only those nuclei with well-measured spins. We will explore a wider range of nuclei and adopt a more recent AME dataset in a later paper.

Using `pynucastro`, we create an `NSENetwork` with our set of nuclei. This can then solve the NSE constraint equations and give us the equilibrium state. We then create a grid of density, temperature, and electron fraction. In all, we use 101 temperature points, equally spaced in logarithm between $T = 10^{9.4}$ K and $T = 10^{10.4}$ K, 61 density points equally spaced in logarithm between $\rho = 10^7$ g cm $^{-3}$ and $\rho = 10^{10}$ g cm $^{-3}$, and 29 Y_e points, linearly spaced between $Y_e = 0.43$ and $Y_e = 0.5$. These correspond to spacings:

$$\Delta \log(T/1 \text{ K}) = 0.01 \quad (\text{A1})$$

$$\Delta \log(\rho/1 \text{ g cm}^{-3}) = 0.05 \quad (\text{A2})$$

$$\Delta \log Y_e = 0.0025 \quad (\text{A3})$$

This fine spacing was needed to get the second-order convergence in our test problem. At each grid point, we compute the NSE state, X_k^{NSE} . The NSE state will evolve as electron captures and β -decays take place and alter Y_e . We can compute this evolution by calling the RHS of the network with X_k^{NSE} :

$$\dot{\omega}_{k,\text{weak}} = \mathcal{F}_{\text{weak}}\{\dot{\omega}_k(\rho, T, X_k^{\text{NSE}})\} \quad (\text{A4})$$

where $\mathcal{F}_{\text{weak}}\{\}$ represents a filter on the rates that only considers the tabulated weak rates. In `pynucastro`, this filtering is done by passing a `rate_filter` function to `RateCollection.evaluate_ydots()` that only acts on the tabulated weak rates.

We store the mean molecular weight of the NSE state:

$$\bar{A} = \sum_k \frac{X_k^{\text{NSE}}}{A_k} \quad (\text{A5})$$

the average binding energy per nucleon of the NSE state:

$$\left\langle \frac{B}{A} \right\rangle = \sum_k \frac{X_k^{\text{NSE}} B_k}{A_k} \quad (\text{A6})$$

the evolution of the electron fraction:

$$\dot{Y}_e = \sum_k \frac{\dot{\omega}_{k,\text{weak}} Z_k}{A_k} \quad (\text{A7})$$

the evolution of the binding energy / nucleon due to weak reactions:

$$\left[\frac{d\langle B/A \rangle}{dt} \right]_{\text{weak}} = -\bar{A}^2 \sum_k \frac{\dot{\omega}_{k,\text{weak}} B_k}{A_k} \quad (\text{A8})$$

and the neutrino loss rate:

$$\epsilon_\nu = \sum_{r \in \text{rates}} Y_r \epsilon_{\nu r}(\rho Y_e, T) \quad (\text{A9})$$

where Y_r is the molar abundance of the nucleus that participates in the decay or capture in rate r .

Finally, we then bin the full set of nuclei down to the 19 we store on the grid:

$$\tilde{X}_k = \text{bin}(\{X_j^{\text{NSE}}\}) \quad (\text{A10})$$

This binning is handled automatically in the `pynucastro Composition.bin_as()` function and seeks to add each NSE nucleus's mass fraction to the corresponding `aprox19` mass fraction by finding the lightest `aprox19` nucleus with an atomic mass greater than or equal to the mass of the NSE nucleus. In the case of multiple matches, we then consider the proton number. We make one exception here, as in [Ma et al. \(2013\)](#), and do not add anything to ^{56}Ni except for the NSE abundance of ^{56}Ni . This is due to the role of ^{56}Ni in lightcurves (although not really needed for this application). We also note that the `aprox19` network includes both ^1H and protons with the former participating in H burning and the latter in photodisintegration links in the heavy elements. This is done to reduce the coupling in the network and simplify the linear algebra. For our NSE state, we only map into the protons.

REFERENCES

- Almgren, A., Sazo, M. B., Bell, J., et al. 2020, *Journal of Open Source Software*, 5, 2513, doi: [10.21105/joss.02513](https://doi.org/10.21105/joss.02513)
- Almgren, A. S., Bell, J. B., Nonaka, A., & Zingale, M. 2008, *ApJ*, 684, 449
- Almgren, A. S., Beckner, V. E., Bell, J. B., et al. 2010, *ApJ*, 715, 1221, doi: [10.1088/0004-637X/715/2/1221](https://doi.org/10.1088/0004-637X/715/2/1221)
- AMReX-Astro initial_models team, Boyd, B., Smith Clark, A., Willcox, D., & Zingale, M. 2024, *AMReX-Astro/initial_models: Release 24.03*, 24.03, Zenodo, doi: [10.5281/zenodo.10827428](https://doi.org/10.5281/zenodo.10827428)
- Arnett, W. D., & Meakin, C. 2011, *ApJ*, 733, 78, doi: [10.1088/0004-637X/733/2/78](https://doi.org/10.1088/0004-637X/733/2/78)
- Brown, P. N., Byrne, G. D., & Hindmarsh, A. C. 1989, *SIAM J. Sci. Stat. Comput.*, 10, 1038
- Bryan, G. L., Norman, M. L., Stone, J. M., Cen, R., & Ostriker, J. P. 1995, *Computer Physics Communications*, 89, 149, doi: [10.1016/0010-4655\(94\)00191-4](https://doi.org/10.1016/0010-4655(94)00191-4)
- Chabrier, G., & Potekhin, A. Y. 1998, *Phys. Rev. E*, 58, 4941, doi: [10.1103/PhysRevE.58.4941](https://doi.org/10.1103/PhysRevE.58.4941)
- Chatzopoulos, E., Couch, S. M., Arnett, W. D., & Timmes, F. X. 2016, *ApJ*, 822, 61, doi: [10.3847/0004-637X/822/2/61](https://doi.org/10.3847/0004-637X/822/2/61)
- Colella, P. 1990, *Journal of Computational Physics*, 87, 171, doi: [10.1016/0021-9991\(90\)90233-Q](https://doi.org/10.1016/0021-9991(90)90233-Q)
- Colella, P., & Woodward, P. R. 1984, *Journal of Computational Physics*, 54, 174, doi: [10.1016/0021-9991\(84\)90143-8](https://doi.org/10.1016/0021-9991(84)90143-8)
- Couch, S. M., Chatzopoulos, E., Arnett, W. D., & Timmes, F. X. 2015, *ApJL*, 808, L21, doi: [10.1088/2041-8205/808/1/L21](https://doi.org/10.1088/2041-8205/808/1/L21)
- Dutt, A., Greengard, L., & Rokhlin, V. 2000, *BIT Numerical Mathematics*, 40, 241, doi: [10.1023/A:102233890](https://doi.org/10.1023/A:102233890)
- Eiden, K., Zingale, M., Harpole, A., et al. 2020, *The Astrophysical Journal*, 894, 6, doi: [10.3847/1538-4357/ab80bc](https://doi.org/10.3847/1538-4357/ab80bc)
- Fan, D., Nonaka, A., Almgren, A. S., Harpole, A., & Zingale, M. 2019, *ApJ*, 887, 212, doi: [10.3847/1538-4357/ab4f75](https://doi.org/10.3847/1538-4357/ab4f75)
- Fields, C. E., & Couch, S. M. 2020, *ApJ*, 901, 33, doi: [10.3847/1538-4357/abada7](https://doi.org/10.3847/1538-4357/abada7)
- . 2021, *ApJ*, 921, 28, doi: [10.3847/1538-4357/ac24fb](https://doi.org/10.3847/1538-4357/ac24fb)
- Fryxell, B., Olson, K., Ricker, P., et al. 2000, *ApJS*, 131, 273
- Gilet, C., Almgren, A. S., Bell, J. B., et al. 2013, *ApJ*, 773, 137, doi: [10.1088/0004-637X/773/2/137](https://doi.org/10.1088/0004-637X/773/2/137)
- Giraud, S., Zegers, R. G. T., Brown, B. A., et al. 2022, *Phys. Rev. C*, 105, 055801, doi: [10.1103/PhysRevC.105.055801](https://doi.org/10.1103/PhysRevC.105.055801)
- Harris, C. R., Millman, K. J., van der Walt, S. J., et al. 2020, *Nature*, 585, 357, doi: [10.1038/s41586-020-2649-2](https://doi.org/10.1038/s41586-020-2649-2)
- Heger, A., Woosley, S. E., Martínez-Pinedo, G., & Langanke, K. 2001, *ApJ*, 560, 307, doi: [10.1086/324092](https://doi.org/10.1086/324092)
- Hix, W. R., & Meyer, B. S. 2006, *NuPhA*, 777, 188, doi: [10.1016/j.nuclphysa.2004.10.009](https://doi.org/10.1016/j.nuclphysa.2004.10.009)

- Huang, W. J., Audi, G., Wang, M., et al. 2017, Chinese Physics C, 41, 030002, doi: [10.1088/1674-1137/41/3/030002](https://doi.org/10.1088/1674-1137/41/3/030002)
- Hunter, J. D. 2007, Computing in Science and Engg., 9, 90, doi: [10.1109/MCSE.2007.55](https://doi.org/10.1109/MCSE.2007.55)
- Itoh, N., Hayashi, H., Nishikawa, A., & Kohyama, Y. 1996, ApJS, 102, 411, doi: [10.1086/192264](https://doi.org/10.1086/192264)
- Johnson, P., Zingale, M., Johnson, E. T., Smith, A., & Niemeyer, K. E. 2023, Research Notes of the AAS, 7, 282, doi: [10.3847/2515-5172/ad175d](https://doi.org/10.3847/2515-5172/ad175d)
- Jones, E., Oliphant, T., Peterson, P., et al. 2001–, SciPy: Open source scientific tools for Python. <http://www.scipy.org/>
- Katz, M. P., Zingale, M., Calder, A. C., et al. 2016, ApJ, 819, 94, doi: [10.3847/0004-637X/819/2/94](https://doi.org/10.3847/0004-637X/819/2/94)
- Kondev, F., Wang, M., Huang, W., Naimi, S., & Audi, G. 2021, Chinese Physics C, 45, 030001, doi: [10.1088/1674-1137/abddae](https://doi.org/10.1088/1674-1137/abddae)
- Kuhlen, M., Woosley, S. E., & Glatzmaier, G. A. 2006, ApJ, 640, 407, doi: [10.1086/500105](https://doi.org/10.1086/500105)
- Kushnir, D., & Katz, B. 2020, Monthly Notices of the Royal Astronomical Society, 493, 5413, doi: [10.1093/mnras/staa594](https://doi.org/10.1093/mnras/staa594)
- Langanke, K., & Martínez-Pinedo, G. 2001, Atomic Data and Nuclear Data Tables, 79, 1, doi: [10.1006/adnd.2001.0865](https://doi.org/10.1006/adnd.2001.0865)
- Ma, H., Woosley, S. E., Malone, C. M., Almgren, A., & Bell, J. 2013, ApJ, 771, 58, doi: [10.1088/0004-637X/771/1/58](https://doi.org/10.1088/0004-637X/771/1/58)
- McCorquodale, P., & Colella, P. 2011, Communications in Applied Mathematics and Computational Science, 6, 1
- Meurer, A., Smith, C. P., Paprocki, M., et al. 2017, PeerJ Computer Science, 3, e103, doi: [10.7717/peerj-cs.103](https://doi.org/10.7717/peerj-cs.103)
- Miller, G. H., & Colella, P. 2002, Journal of Computational Physics, 183, 26, doi: [10.1006/jcph.2002.7158](https://doi.org/10.1006/jcph.2002.7158)
- Minion, M. L. 2003, Commun. Math. Sci., 1, 471. <https://projecteuclid.org:443/euclid.cms/1250880097>
- Mocák, M., Campbell, S. W., Müller, E., & Kifonidis, K. 2010, A&A, 520, A114, doi: [10.1051/0004-6361/201014461](https://doi.org/10.1051/0004-6361/201014461)
- Müller, B. 2020, Living Reviews in Computational Astrophysics, 6, 3, doi: [10.1007/s41115-020-0008-5](https://doi.org/10.1007/s41115-020-0008-5)
- Müller, B., Melson, T., Heger, A., & Janka, H.-T. 2017, MNRAS, 472, 491, doi: [10.1093/mnras/stx1962](https://doi.org/10.1093/mnras/stx1962)
- Navó, G., Reichert, M., Obergaulinger, M., & Arcones, A. 2023, ApJ, 951, 112, doi: [10.3847/1538-4357/acd640](https://doi.org/10.3847/1538-4357/acd640)
- Nethercote, N., & Seward, J. 2007, in Proceedings of the 28th ACM SIGPLAN Conference on Programming Language Design and Implementation, PLDI '07 (New York, NY, USA: ACM), 89–100, doi: [10.1145/1250734.1250746](https://doi.org/10.1145/1250734.1250746)
- Oliphant, T. E. 2007, Computing in Science and Engg., 9, 10, doi: [10.1109/MCSE.2007.58](https://doi.org/10.1109/MCSE.2007.58)
- Paxton, B., Bildsten, L., Dotter, A., et al. 2011, ApJS, 192, 3, doi: [10.1088/0067-0049/192/1/3](https://doi.org/10.1088/0067-0049/192/1/3)
- Paxton, B., Schwab, J., Bauer, E. B., et al. 2018, ApJS, 234, 34, doi: [10.3847/1538-4365/aaa5a8](https://doi.org/10.3847/1538-4365/aaa5a8)
- Rauscher, T. 2003, The Astrophysical Journal Supplement Series, 147, 403, doi: [10.1086/375733](https://doi.org/10.1086/375733)
- Rauscher, T., Heger, A., Hoffman, R. D., & Woosley, S. E. 2002, ApJ, 576, 323, doi: [10.1086/341728](https://doi.org/10.1086/341728)
- Rauscher, T., Thielemann, F.-K., & Kratz, K.-L. 1997, Phys. Rev. C, 56, 1613, doi: [10.1103/PhysRevC.56.1613](https://doi.org/10.1103/PhysRevC.56.1613)
- Seitenzahl, I. R., Townsley, D. M., Peng, F., & Truran, J. W. 2009, Atomic Data and Nuclear Data Tables, 95, 96, doi: [10.1016/j.adt.2008.08.001](https://doi.org/10.1016/j.adt.2008.08.001)
- Smith Clark, A., Johnson, E. T., Chen, Z., et al. 2023, arXiv e-prints, arXiv:2311.17357, doi: [10.48550/arXiv.2311.17357](https://doi.org/10.48550/arXiv.2311.17357)
- . 2022, arXiv e-prints, arXiv:2210.09965. <https://arxiv.org/abs/2210.09965>
- Strang, G. 1968, SIAM J. Numerical Analysis, 5, 506
- Timmes, F. X., & Swesty, F. D. 2000, ApJS, 126, 501, doi: [10.1086/313304](https://doi.org/10.1086/313304)
- Townsley, D. M., Calder, A. C., Asida, S. M., et al. 2007, ApJ, 668, 1118, doi: [10.1086/521013](https://doi.org/10.1086/521013)
- Turk, M. J., Smith, B. D., Oishi, J. S., et al. 2011, ApJS, 192, 9, doi: [10.1088/0067-0049/192/1/9](https://doi.org/10.1088/0067-0049/192/1/9)
- van der Walt, S., Colbert, S. C., & Varoquaux, G. 2011, Computing in Science & Engineering, 13, 22, doi: [10.1109/MCSE.2011.37](https://doi.org/10.1109/MCSE.2011.37)
- Varma, V., & Mueller, B. 2023, arXiv e-prints, arXiv:2307.04833, doi: [10.48550/arXiv.2307.04833](https://doi.org/10.48550/arXiv.2307.04833)
- Virtanen, P., Gommers, R., Oliphant, T. E., et al. 2020, Nature Methods, 17, 261, doi: [10.1038/s41592-019-0686-2](https://doi.org/10.1038/s41592-019-0686-2)
- Wang, M., Audi, G., Kondev, F. G., et al. 2017, Chinese Physics C, 41, 030003, doi: [10.1088/1674-1137/41/3/030003](https://doi.org/10.1088/1674-1137/41/3/030003)
- Weaver, T. A., Zimmerman, G. B., & Woosley, S. E. 1978, ApJ, 225, 1021, doi: [10.1086/156569](https://doi.org/10.1086/156569)

- Willcox, D. E., & Zingale, M. 2018, *Journal of Open Source Software*, 3, 588, doi: [10.21105/joss.00588](https://doi.org/10.21105/joss.00588)
- Yadav, N., Müller, B., Janka, H. T., Melson, T., & Heger, A. 2020, *ApJ*, 890, 94, doi: [10.3847/1538-4357/ab66bb](https://doi.org/10.3847/1538-4357/ab66bb)
- Yoshida, T., Takiwaki, T., Aguilera-Dena, D. R., et al. 2021a, *Monthly Notices of the Royal Astronomical Society: Letters*, 506, L20, doi: [10.1093/mnrasl/slab067](https://doi.org/10.1093/mnrasl/slab067)
- Yoshida, T., Takiwaki, T., Kotake, K., et al. 2019, *The Astrophysical Journal*, 881, 16, doi: [10.3847/1538-4357/ab2b9d](https://doi.org/10.3847/1538-4357/ab2b9d)
- . 2021b, *The Astrophysical Journal*, 908, 44, doi: [10.3847/1538-4357/abd3a3](https://doi.org/10.3847/1538-4357/abd3a3)
- Zhang, W., Almgren, A., Beckner, V., et al. 2019, *Journal of Open Source Software*, 4, 1370, doi: [10.21105/joss.01370](https://doi.org/10.21105/joss.01370)
- Zingale, M., Katz, M. P., Bell, J. B., et al. 2019, *arXiv e-prints*, arXiv:1908.03661. <https://arxiv.org/abs/1908.03661>
- Zingale, M., Katz, M. P., Nonaka, A., & Rasmussen, M. 2022, *The Astrophysical Journal*, 936, 6, doi: [10.3847/1538-4357/ac8478](https://doi.org/10.3847/1538-4357/ac8478)
- Zingale, M., Katz, M. P., Willcox, D. E., & Harpole, A. 2021, *Research Notes of the AAS*, 5, 71, doi: [10.3847/2515-5172/abf3cb](https://doi.org/10.3847/2515-5172/abf3cb)